Advanced Review

Magnetic resonance relaxation induced by superparamagnetic particles used as contrast agents in magnetic resonance imaging: a theoretical review

Quoc Lam Vuong,[1]* Pierre Gillis,[1] Alain Roch[2] and Yves Gossuin[1]

Superparamagnetic nanoparticles are used as contrast agents in magnetic resonance imaging and allow, for example, the detection of tumors or the tracking of stem cells *in vivo*. By producing magnetic inhomogeneities, they influence the nuclear magnetic relaxation times, which results in a darkening, on the image, of the region containing these particles. A great number of studies have been devoted to their magnetic properties, to their synthesis and to their influence on nuclear magnetic relaxation. The theoretical and fundamental understanding of the behavior of these particles is a necessary step in predicting their efficiency as contrast agents, or to be able to experimentally obtain some of their properties from a nuclear magnetic resonance measurement. Many relaxation models have been published, and choosing one of them is not always easy, many parameters and conditions have to be taken into account. Relaxation induced by superparamagnetic particles is generally attributed to an outersphere relaxation mechanism. Each model can only be used under specific conditions (motional averaging regime, static regime, high magnetic field, etc.) or for a particular sequence (Carr-Purcell-Meiboom-Gill, spin echo, free-induction decay, nuclear magnetic relaxation dispersion profile, etc.). The parameters included in the equations must be carefully interpreted. In some more complex conditions, simulations are necessary to be able to predict the relaxation rates. A good agreement is usually observed between the theoretical predictions and the experimental results, although some data still cannot be fully understood, such as the dependence of the transverse relaxation on the magnetic field.

How to cite this article:
WIREs Nanomed Nanobiotechnol 2017, e1468. doi: 10.1002/wnan.1468

INTRODUCTION

For the last few decades, research on superparamagnetic nanoparticles (SPM NPs) has led to a significant number of applications which have become, or are promised to be, essential in the biomedical field. They can be used as magnetic separators using a suitable vectorization,[1] can perform tissue regeneration,[2,3] can be used as a heating source for hyperthermia[4] or can be directly detected to reveal tumor cells or coronary vessels with magnetic particle imaging (MPI, see Box 1).[5]

SPM NPs—mainly represented by iron oxide nanoparticles[6,7]—are also used as contrast agents (CA) in magnetic resonance imaging (MRI). In MRI, CA can be categorized into positive or

*Correspondence to: quoclam.vuong@umons.ac.be

[1]Biomedical Physics Unit, UMONS, Mons, Belgium

[2]Faculty of Medicine, UMONS, Mons, Belgium

Conflict of interest: The authors have declared no conflicts of interest for this article.

BOX 1

A NEW IMAGING TECHNIQUE BASED ON SPM NPs: MPI

While SPM NPs are indirectly detected by their influence on water protons in MRI, a new and recent imaging technique called MPI has been elaborated based on their direct detection.[5,119] The principle of MPI is to put the SPM NPs under an oscillatory exciting magnetic field: if the oscillation is slower than the magnetic NP relaxation, the NP magnetic magnetization will follow the oscillation. The amplitude of the excitation field is chosen as larger than the magnetic field at which the particles saturate, which means the SPM response is not a pure sine oscillation. This specific response can thus be exploited to distinguish regions without SPM NPs and regions containing SPM NPs. Additional gradients and more complex excitations can be used to localize the signal and the SPM NP concentration and to obtain a gray scaled image.

MPI is therefore an imaging tracer-based method which is able to provide a quantitative measurement of SPM NP concentration with high sensitivity and is characterized by high spatial (<1 mm) and temporal (<0.1 s) resolutions. As in MRI, MPI only uses non-ionizing radiation meaning that it is safe for the patient. Since it is a recent imaging technique, only a few studies focus on the *in vivo* medical application of this technique. Preliminary studies for cardiovascular blood flow imaging,[120] cell labeling and tracking[121–123] have provided promising results for the use of MPI in future human diagnosis.

negative types. For example, gadolinium chelates shorten the nuclear longitudinal relaxation time, which results in a signal amplification with a suited imaging sequence, making them appearing brighter in the image. These are called 'positive contrast agents.' SPM NPs increase the transverse relaxation rate by producing magnetic field inhomogeneities in their surroundings. Whereas specific MRI sequences can produce positive contrast with SPM NPs,[8–11] SPM NPs appear dark in conventional MRI sequences, therefore, they belong in the negative CA category. Compared to gadolinium compounds, SPM NPs have the advantage of bearing a huge magnetic moment which produces a large dipolar magnetic field and of being non-toxic in the current state of knowledge.

Extensive research has been done on modeling and quantitatively understanding the influence of SPM NPs on proton relaxation rates. While the theoretical models are quite abstract and necessitate advanced mathematical tools to be demonstrated, they are not only useful from a fundamental point of view, as they allow the extraction of interesting quantities from the relaxation rate measurements, such as particle concentration, size, and magnetization. Correct modeling of the relaxation mechanisms can lead to the quantification of SPM NP labeled cells, the characterization of an SPM NP after a synthesis process or can help to define the optimal parameters for their use as CA.

In this review, different theoretical models of the proton nuclear magnetic relaxation induced by SPM NPs will be presented and discussed. An emphasis will be put on their correct use in different experimental conditions and on the rigorous definition of each parameter.

SUPERPARAMAGNETIC PARTICLES

In this section, the magnetic properties of SPM NPs will be discussed. Before reading further, it is important to note that the magnetic moment discussed in this section belongs to the SPM NP itself. It is often mentioned in the literature as 'electronic' or 'SPM' magnetic moment which must be distinguished from the proton magnetic moment arising from its spin. The signal in MRI or nuclear magnetic resonance (NMR) is exclusively due to the proton spins.

Superparamagnetism

A magnet is characterized by its magnetic moment, a vector whose magnitude indicates its magnetic intensity and whose direction points from south to north poles. The ratio between the amplitude of the magnetic moment and the volume of a material defines its 'magnetization.' A magnet is either ferromagnetic or ferrimagnetic: its electron spins interact with the applied external magnetic field (Zeeman interaction) as well as with each other (exchange interaction). In a ferromagnetic material, each electron spin tends to be aligned with its neighbor. A ferrimagnetic material is composed of electrons, which tend to be unequally anti-aligned with their neighbors, giving rise to a non-null total magnetic moment.

A magnet is featured by a magnetic hysteresis curve (Figure 1(a)): its magnetization dependence on

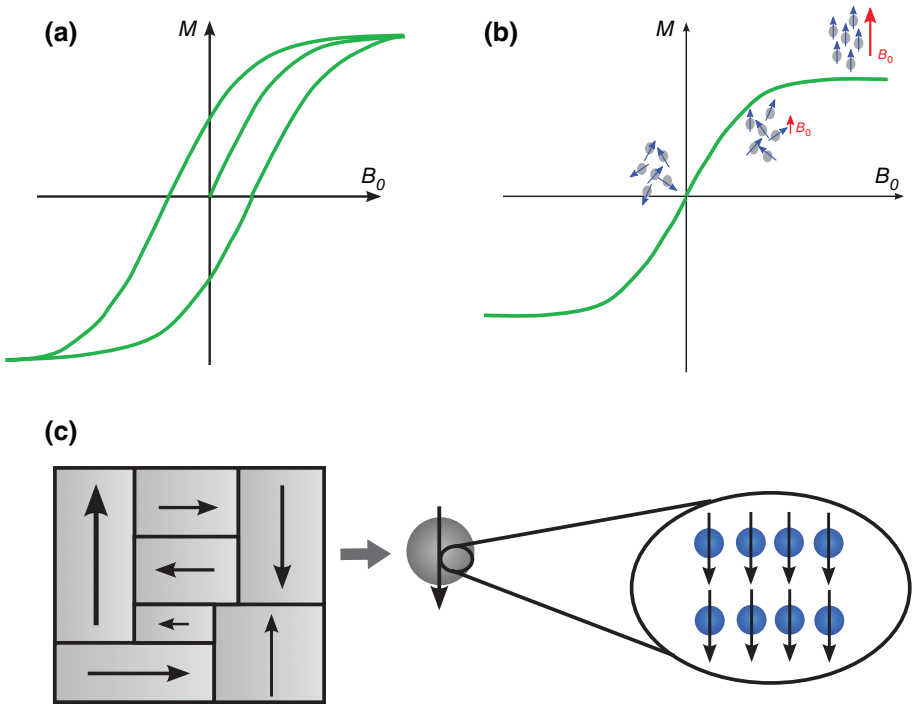

FIGURE 1 | (a) Hysteresis curve of a ferro- or ferrimagnetic material. (b) Magnetic Langevin curve of a sample containing superparamagnetic nanoparticles. (c) A magnetic material is composed of Weiss domains. The arrows represent the electronic moment or spin of each structure. A superparamagnetic nanoparticle (SPM NP) is a particle composed of a single magnetic domain in which the electron spins are all aligned in the same direction.

the applied magnetic field presents a remnant magnetization and an irreversible evolution.[12] These materials are composed of magnetic domains, called 'Weiss domains,' in which the electron spins are aligned with each other (Figure 1(c)). It is important to note that the magnetic moment of these particles is far larger than the proton magnetic signal detected in NMR, which is produced by the nuclei.

A superparamagnetic particle is defined as a magnetic particle which[13,14]

1. is composed of a single Weiss domain
2. has no remnant magnetization and thus presents a reversible magnetization curve

Property (1) leads to a huge particle magnetic moment compared to the magnetic moment of a single magnetic ion. As all the electron spins are always aligned with each other in a single magnetic domain, the magnitude $|\vec{\mu}_{\mathrm{SPM}}|$ of the magnetic moment of a single SPM NP is always constant. Property (2) means that whatever the particle history is, the measurement always provides the equilibrium state of the sample (-Figure 1(b)). Thus, at zero applied field, the magnetic moment of one nanoparticle in the sample jumps from one direction to another so that its magnetic moment is time averaged to zero. This is only possible if the characteristic relaxation time of the SPM NPs of the sample is very small compared to the measurement time.

Anisotropy Energy

The magnetic moment of an SPM NP is preferentially aligned in specific directions. These directions depend on several parameters, such as the crystallographic structure and shape of the particle. In the simplest case of uniaxial anisotropy, there is only one easy-direction and the tendency for the magnetic moment to be aligned—or anti-aligned—with this axis depends on its anisotropy energy

$$H_A = KV\sin^2\theta \tag{1}$$

where K is the anisotropy constant proper to the material, V is the particle volume, and θ is the angle between the anisotropy axis and the magnetic moment vector. The energy is minimum when the magnetic moment is aligned ($\theta = 0°$) or anti-aligned ($\theta = 180°$) with the easy axis and flipping from one

minimum position to another requires overcoming an energy barrier of KV.

Néel and Rotational Brownian Relaxations

To be considered as superparamagnetic, the relaxation of the magnetic moment of the NP must be faster than the measurement time. Two main relaxation processes occur in a liquid sample containing SPM NPs: the Néel and the rotational Brownian relaxations.

If the thermal fluctuations are large enough, the magnetic moment of an SPM NP has sufficient energy to overcome the anisotropy energy barrier and can jump from one minimum-energy position to another—leading to a null time average magnetization, if the measurement time is long enough. This characteristic jumping time is called the 'Néel relaxation time,'[15] it exponentially depends on the nanoparticle volume

$$\tau_N = \tau_0 e^{KV/k_B T} \quad (2)$$

where T is the sample temperature and k_B is the Boltzmann constant. τ_0 is usually considered as a constant depending on the considered material at first approximation, but actually depends on several particle parameters, such as its volume, anisotropy energy, temperature, etc.[13] Equation (2) is also only strictly valid when assuming a zero applied magnetic field and only for non-interacting particles. In case of interparticle interactions (occurring at high particle concentrations), a Vogel-Fulcher model must be used. The Néel relaxation is dominant when the Néel time is short, i.e., when the particle is sufficiently small or when the temperature is high enough.

In a liquid, SPM NPs are submitted to collisions with the solvent molecules which makes the particle rotate randomly. The corresponding rotational Brownian relaxation time is given by

$$\tau_B = \frac{3\eta V_H}{k_B T} \quad (3)$$

where η is the dynamic viscosity of the carrier fluid and V_H is the hydrodynamic volume of the particle.[16] This relaxation is efficient when the anisotropy energy is very high: in this case, the magnetic moment of the NP is blocked along its easy axis since the Néel relaxation time is enormous. The only way to reorient the magnetic moment of the particle is to physically rotate the NP. Of course, when particles are not in a liquid (e.g., if they are in ice, in a dried powder), no Brownian relaxation occurs and only the Néel relaxation has to be considered. This rotational relaxation is also less effective when the particles are constrained in tissues.

When both relaxation mechanisms are of the same order of magnitude, an effective relaxation time τ can be introduced and it obeys the equation

$$\frac{1}{\tau} = \frac{1}{\tau_N} + \frac{1}{\tau_B}. \quad (4)$$

τ can be interpreted as the characteristic time for the system to exponentially evolve from its initial state to the equilibrium state. Equation (4) shows that it is the shortest relaxation time which is dominant. To know if a particle is in the superparamagnetic regime, one only needs to compare the shortest relaxation time to the measurement time.

Magnetization Curve

As shown in Figure 1(b), when a sample containing superparamagnetic particles is exposed to an increasing magnetic field, the sample magnetization increases up to a saturation value, corresponding to the case in which the magnetic moment of each particle is aligned with the external magnetic field. This curve is usually well described by a Langevin function

$$L(x) = \coth x - \frac{1}{x}; x = \frac{\mu_{SPM} B_0}{k_B T} \quad (5)$$

where $\vec{B}_0$ is the external field and $\vec{\mu}_{SPM}$ is the SPM NP's magnetic moment. This equation is obtained by considering the thermal energy and the coupling energy between the magnetic moments and the external field $\vec{B}_0$

$$H_0 = -\vec{\mu}_{SPM} \cdot \vec{B}_0. \quad (6)$$

The Langevin function neglects the anisotropy energy and is thus only valid if the anisotropy energy is very small compared to the thermal fluctuations. For larger anisotropy energy, deviation from the Langevin law can be observed.[17,18]

Iron Oxides

Among all the SPM NPs used in the medical field, iron oxides—especially ferrimagnetic magnetite and maghemite—are certainly the most popular CAs. Magnetite (Fe_3O_4) is a hard black mineral while maghemite (γ-Fe_3O_4) appears red-brown, and has the same crystalline structure as magnetite, but with cation vacancies. As maghemite can result from the oxidation of magnetite, pure magnetite does not exist in the medical field, where water is omnipresent and causes the oxidation of magnetite. However, the

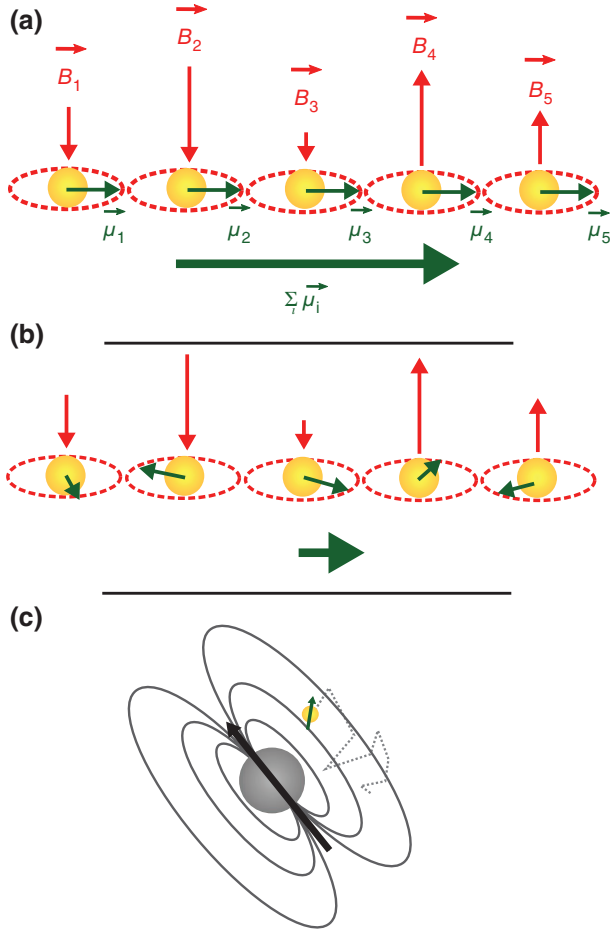

FIGURE 2 | (a) Red arrows represent local magnetic fields and green arrows the proton spins. Each proton is exposed to its own local magnetic field. After the 90°-pulse of a T_2* sequence, all the proton spins are aligned in the transverse plane and the proton magnetization is thus maximum. (b) After a while, with each proton rotating at its own frequency and neglecting proton diffusion, a dephasing occurs and the magnetization is zero. (c) In a more realistic case, such as the superparamagnetic nanoparticle (SPM NP) case, magnetic inhomogeneities are produced by the SPM NP dipolar field and fluctuations come from the proton diffusion and the SPM magnetic moment fluctuation due to Néel or Brownian rotational relaxations.

difference between these two iron oxides does not tremendously influence the relaxation properties.

The size of a magnetite Weiss domain is about 0.1 μm. For magnetite, $\tau_0 \approx 10^{-9}$ s and $K \approx 13{,}500$ J m^{-3} and Eq. (2) leads to a Néel time of 700 years for a 15nm-particle radius and to 0,5 ms for a 10 nm-particle radius at 310 K: the Néel time of a particle is strongly dependent on its size and is the dominant relaxation mechanism for particles smaller than 10 nm. For larger particles, the Brownian relaxation will be dominant.

NUCLEAR MAGNETIC RELAXATION INDUCED BY SUPERPARAMAGNETIC PARTICLES

When an NMR experiment is carried out on an aqueous sample containing SPM NPs, the corresponding longitudinal and transverse nuclear magnetic relaxation times T_1 and T_2 get shorter compared to the sample without any SPM NPs. While a fully quantum theory should be used to rigorously model what microscopically happens in the sample, in the case of SPM NPs, a classical view is enough to qualitatively understand the relaxation mechanisms involved in the sample.[19,20]

Microscopic Origins: Fundamental Hypothesis

Magnetic Inhomogeneities and Fluctuations

In a classical view, a proton spin can be represented by a nuclear magnetic moment vector. Exposed to a local magnetic field $\vec{B}_{loc}$, a single proton magnetic moment rotates around the field at the local Larmor frequency $\nu_p = \gamma_p B_{loc}/2\pi$ where γ_p is the proton gyromagnetic ratio. Relaxation is caused by (1) the presence of magnetic field inhomogeneities and (2) the fact that each single proton is exposed to magnetic fluctuations (Figure 2(a) and (b)). These two conditions imply a possibly irreversible proton spin dephasing which results in an evolution of the average proton magnetization of the sample.

Outersphere Mechanism

In the case of SPM NPs, most of the theoretical models postulate that relaxation arises from the magnetic inhomogeneities produced by the dipolar magnetic field of the particles. This dipolar magnetic field depends on the magnetic moment of the SPM NP. In an aqueous sample, each proton experiences magnetic fluctuations because of (1) its free bulk diffusion in these magnetic inhomogeneities (this is called the outersphere mechanism, see Figure 2(c)) and (2) the Néel and Brownian relaxation of the SPM magnetization.

Fundamental Assumptions

These two simple assumptions actually hide other hypotheses that the reader must take into account before using the models:

- Water diffusion is modeled by the diffusion equation, and water molecules are supposed to approach the particle at a minimal distance R_{NMR} (a spherical symmetry is supposed). Thus the 'radius' of the SPM NP obtained in NMR is

not necessarily the same as the radius obtained in transmission electron microscopy (TEM), i.e., the real radius of the SPM nanocrystal. For example, if the NP is covered by an impermeable coating, R_{NMR} will be the sum of coating thickness and of the NP crystal radius.[21–23]

- Concentration of SPM NPs in water is supposed to be very low and NPs are supposed to be homogeneously distributed in the sample. In case of aggregation of SPM NPs, a modification of the standard theories presented in this section is absolutely necessary.
- The SPM magnetic moment is supposed to be submitted to a Néel and/or Brownian rotation relaxation depending on the considered sample. It is also supposed to rotate around the magnetic field at the electronic Larmor frequency at low anisotropy energy.
- The SPM magnetic moment is supposed to follow a Boltzmann distribution—i.e., it tends to get aligned with the applied magnetic field.
- For the sake of calculus simplicity, only uniaxial anisotropy is considered.

These assumptions were progressively introduced into the models to refine the understanding of the different experimental data. Renshaw et al. were the first to suggest applying the outersphere mechanism for SPM samples[24] based on the relaxation models of paramagnetic ions.[25–28] Gillis and Koenig extended the model for all magnetic fields.[29] An assumption about the dependence of the SPM magnetization on the applied magnetic field was then introduced by Koenig and Brown.[30] Roch et al. proposed the first model which fitted experimental data for high anisotropy[31] and which inspired Koenig and Kellar for a low anisotropy model[32]—failing to completely fit the data.[33] A full quantum model was then proposed by Roch et al.[34] which was able to fit experimental data presenting high or low anisotropy. More recently, a new model has been presented by Levy et al.,[35] which is more suited to high anisotropy SPM NPs. Considerable theoretical work has also been achieved for the transverse relaxation rate at high fields—which is easier to model—using simulations or different mathematical methods; experimental data were successfully reproduced.[36–43] These models will be explained in more detail in the next sections and are summarized in Table 1.

NMRD Profiles: Longitudinal Relaxation

Nuclear magnetic relaxation dispersion (NMRD) profiles are curves describing the dependence of the relaxation rates on the applied external magnetic field B_0 (expressed in proton Larmor frequency). From a fundamental point of view, they provide interesting information on the microscopic mechanisms occurring in the sample.[46] In practice, fitting the experimental NMRD data with the right model equations allows the microscopic parameters of the sample to be extracted.

Almost all the current formula used for NMRD profiles are restricted by the 'Redfield condition': they are only valid if the magnetic fluctuations are very fast and if their amplitude is small. In the case of SPM NPs dispersed in water, this condition—called the 'motional averaging regime' (MAR)—is given by

$$\frac{\gamma_p \mu_0 M_{NMR}^{sat}}{3} \frac{R_{NMR}^2}{D} \ll 1 \tag{7}$$

where $\mu_0 = 4\pi \times 10^{-7}$ H m^{-1} is the vacuum magnetic permeability, R_{NMR} is the minimal NP-proton distance of approach, D is the water diffusion coefficient, $\gamma_p = 267{,}522$ rad s^{-1} T^{-1} is the proton gyromagnetic ratio, $M_{crystal}^{sat}$ is the saturation magnetization of the nanocrystal given by

$$M_{NMR}^{sat} = \frac{\mu_{SPM}}{\frac{4}{3}\pi R_{NMR}^3} \tag{8}$$

which is the effective magnetization felt by the protons. The condition in Eq. (7) must always be checked before a fitting of the experimental data.

Low Anisotropy Energy (Dominant Néel Relaxation)

For particles with low and intermediate anisotropy energies, Néel relaxation is fast and dominates the rotational Brownian relaxation (i.e., $\tau_N \ll \tau_R$). In this case, the low anisotropy model[34] can be applied and the longitudinal relaxation rate is given by

$$R_1 = \frac{1}{T_1} = \frac{32\pi}{135}\left(\frac{\mu_0}{4\pi}\right)^2 \mu_{SPM}^2 \gamma_p^2 \frac{C}{R_{SPM} D} R_{Neel}(P, \omega_e, \omega_p, \tau_D, \tau_N, \xi) \tag{9}$$

with

$$R_{Neel}(P, \omega_e, \omega_p, \tau_D, \tau_N, x) = 7P\frac{L(x)}{x} J_F(\omega_e, \tau_D, \tau_N) + \left[7(1-P)\frac{L(x)}{x} + 3\left(1 - 2\frac{L(x)}{x} - L^2(x)\right)\right] J_F(\omega_p, \tau_D, \tau_N) + 3L^2(x) J_A(\omega_p, \tau_D). \tag{10}$$

C is the nanoparticle concentration, i.e., the number of particles per volume (in m^{-3})

TABLE 1 | Summary of the Theoretical Models

	Model Name	Equation Number	Model Conditions—Comments
NMRD	Low Anisotropy Model[34]	R_1: Eq. (9)	MAR condition (Eq. (7))
		$R_2 = R_2^*$: Eq. (17)	Low SPM NP concentration
			No SPM NP aggregation
			Low anisotropy energy/dominant Néel relaxation
			NMRD prediction: can be used to calculate the relaxation at any static magnetic field B_0
	Rigid Dipole Model[35]	R_1: Eq. (14)	MAR condition (Eq. (7))
		$R_2 = R_2^*$: Eq. (19)	Low SPM NP concentration
			No SPM NP aggregation
			High anisotropy energy/dominant Brownian rotational relaxation
			NMRD prediction: can be used to calculate the relaxation at any static magnetic field B_0
	Three-Phase Iron Model[44]	R_1: Eq. (21)	MAR condition (Eq. (7))
		R_2: Eq. (22)	Low SPM NP concentration
			No SPM NP aggregation
			Low anisotropy energy/dominant Néel relaxation
			NMRD prediction: can be used to calculate the relaxation at any static magnetic field B_0
			The SPM NP is supposed to be composed of an SPM, an antiferromagnetic, and a paramagnetic phases
			Ideally requires other measurement methods to extract the values of the additional parameters of the model
CPMG—FID	MAR Scaling Law[45]	Theoretical prediction: Eq. (25)	MAR condition (Eq. (7))
		Empirical scaling law: Eq. (26)	Low SPM NP concentration
			No SPM NP aggregation
			Available only at high applied magnetic field B_0
			In the MAR condition, $R_2 = R_2*$ (if the echo time is longer than the correlation time)
FID	Static Model[39]	R_2^*: Eq. (28)	Static condition (Eq. (27))
			Low SPM NP concentration
			Available only at high applied magnetic field B_0
			Available only for an FID sequence
CPMG	Partial Refocusing Model[37]	R_2: Eq. (29)	Static condition (Eq. (27))
			Low SPM NP concentration
			Available only at high applied magnetic field B_0
			Available only for a CPMG sequence
Spin Echo	Spin Echo Kurz Model[41]	R_2: Eq. (30)	The model should be valid in the static and MAR regimes, but with the parameters used in this article, only the simulation points in the static region were in agreement with the prediction of this model
			Available only at high applied magnetic field B_0
			Available for a spin echo sequence
			The κ parameter can be approximated by Eq. (31) but its exact value is given by the solution of the transcendental Eq. (5) in Ref 41

CPMG, Carr-Purcell-Meiboom-Gill; FID, free-induction decay; MAR, motional averaging regime; NMRD, nuclear magnetic relaxation dispersion; SPM NP, superparamagnetic nanoparticle.

$$C = \frac{N_{SPM}}{V_{sample}}; \tau_D = \frac{R_{NMR}^2}{D} \quad (11)$$

where N_{SPM} is the total number of SPM NPs in the sample, V_{sample} is the sample volume, $x = \mu_{SPM}B_0/k_BT$, $\omega_e = \gamma_e B_0$ is the angular electronic Larmor frequency, $\omega_p = \gamma_p B_0$ is the angular proton Larmor frequency, $\gamma_e = 1.76086\ 10^{11}$ C kg^{-1} is the electronic gyromagnetic ratio, τ_N is the Néel time, P is an empirical parameter which depends on the SPM anisotropy energy.[34,47] In Eq. (10), the Freed and Ayant spectral densities[48,49] are defined as

$$J_F(\omega,\tau_D,\tau_N) = \mathrm{Re}\left(\frac{1+\frac{z^{1/2}}{4}}{1+z^{1/2}+\frac{4z}{9}+\frac{z^{3/2}}{9}}\right) \text{ with } z = \frac{\tau_D}{\tau_N} + \omega\tau_D i \quad (12)$$

$$J_A(\omega,\tau_D) = \frac{1+\frac{5z}{8}+\frac{z^2}{8}}{1+z+\frac{z^2}{2}+\frac{z^3}{6}+\frac{4z^4}{81}+\frac{z^5}{81}+\frac{z^6}{648}} \text{ with } z = \sqrt{2\omega\tau_D} \quad (13)$$

where $Re(z)$ is the real part of the imaginary number z. Equation (9), derived by Roch et al.,[34] is semi-empirical: it is a linear combination of contributions with a zero, and with an infinite anisotropy energies formula. It was able to reproduce the predictions of the full-quantum calculation. A simplified version of their expression (using $Q = 1 - P$ and $\omega_0 = 0$ in Eq. (31) of Ref 34) is proposed here because it is able to reproduce most of the fittings.[50]

Typical curves are shown in Figure 3. Néel relaxation influences only the low-field part of the curve, which increases when the Néel time is larger. The first minimum of the NMRD is due to the anisotropy energy through the empirical parameter P: it disappears if the anisotropy energy is sufficiently high (corresponding to $P = 0$). The increase of the relaxation rate can be attributed to the reorientation of the SPM magnetic moment with the applied magnetic field and is mathematically related to the Langevin function. Then the final decrease of the relaxation rate is caused by the shape of the spectral densities which tend to zero when the Larmor frequencies tend to infinity. The position of the last inflection point is reached when $\omega_p\tau_D = \gamma_I B_0 R_{NMR}^2/D \approx 1$ which gives a visual indication on the proton minimal distance of approach R_{NMR}: the more the inflection point is shifted to the low magnetic field B_0, the larger R_{NMR} is (Figure 3(a)).

In this model, the Néel time is considered as independent of the magnetic field—a strong (and often invalid) assumption. Moreover, it neglects the interaction between the SPM NPs which can influence the Néel time at high particle concentrations.[51] The obtained Néel time from this model has to be carefully interpreted and actually only provides a rough qualitative estimation of its real value[47]—this discrepancy still remains unclear. Another model was also proposed by Levy et al.[35]—it directly introduces the anisotropy energy into the model and takes into account the dependence of the Néel time on the magnetic field. However, it is less easy to implement than the low anisotropy model because of a non-analytical integral.

High Anisotropy Energy (Dominant Brownian Relaxation)

When the anisotropy energy of the SPM NP is very high compared to thermal fluctuations, the SPM magnetic moment is blocked on its anisotropy axis. In this case, Lévy et al. introduced the 'rigid dipole model' which can be applied when the rotational Brownian relaxation is dominant: the longitudinal relaxation rate is then given by

$$R_1 = \frac{1}{T_1} = \frac{16\pi}{135}\left(\frac{\mu_0}{4\pi}\right)^2 \mu_{SPM}^2 \gamma_p^2 \frac{C}{R_{SPM}D} R_{Brown}(x,\omega_p,\tau_D,\tau_\perp,\tau_\parallel) \quad (14)$$

with

$$R_{Brown}(x,\omega_I,\tau_D,\tau_\perp,\tau_\parallel) = \left[14\frac{L(x)}{x}J_F(\omega_I,\tau_D,\tau_\perp) + 6L^2(x)J_A(\omega_I,\tau_D) + 6\left(1-\frac{2L(x)}{x}-L^2(x)\right)J_F(\omega_p,\tau_D,\tau_\parallel)\right] \quad (15)$$

$$\tau_\perp = \frac{2L(x)}{x-L(x)}\tau_B;\ \tau_\parallel = \frac{d\ln L(x)}{d\ln(x)}\tau_B = \frac{x}{L(x)}\left(\frac{1}{x^2}-\frac{1}{\sinh^2(x)}\right)\tau_B;\ \tau_B = \frac{4\pi\eta R_{NMR}^3}{k_BT};\ x = \frac{\mu_{SPM}B_0}{k_BT} \quad (16)$$

where $\eta = 0.6915 \times 10^{-3}$ Pa. s is the water viscosity at 37°C.[52]

Typical NMRD curves of this model are shown in Figure 4: the curves are characterized by a simpler decreasing shape and do not present any maximum.

The inflection point is radius dependent and is shifted to lower magnetic fields for larger radii. The nanoparticle magnetization only influences the magnitude of the curve without changing its shape.

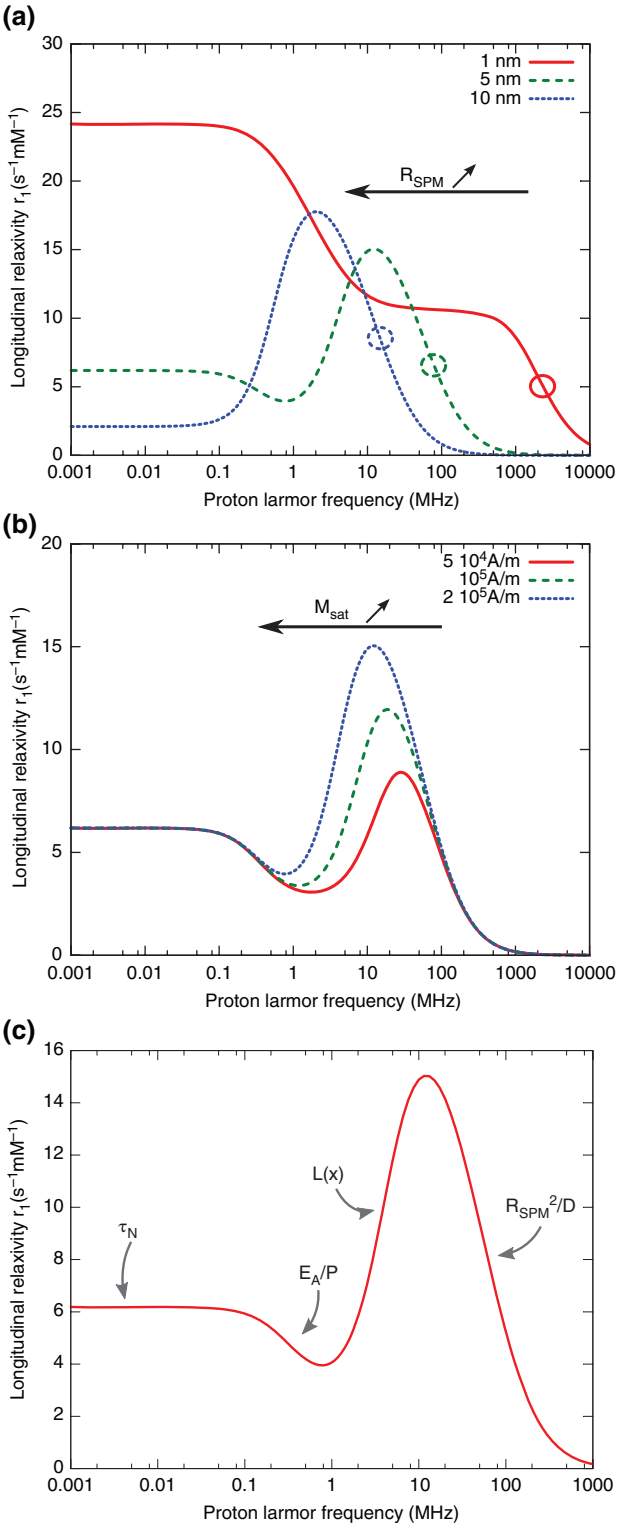

FIGURE 3 | Legend on next column.

NMRD Profiles: Transverse Relaxation

Contrarily to longitudinal NMRD, just a few studies tried to compare the theory and experiments for the transverse relaxation[53–55] while, for SPM NPs, the T_2-contrast is mostly used in MRI. However, the influence of the magnetic field on the transverse relaxation rates had already been studied at intermediate fields 20 years ago.[43] While theoretical predictions are available, significant variations of the transverse relaxation are expected to occur at fields so low that it is technically very difficult to measure the signal decay. In the dominant Néel relaxation model, this is given by[55,56]

$$R_2^* = \frac{1}{T_2^*} = \frac{16\pi}{135}\left(\frac{\mu_0}{4\pi}\right)^2 \mu_{\mathrm{SPM}}^2 \gamma_p^2 \frac{C}{R_{\mathrm{SPM}} D}$$

$$R'_{\mathrm{Neel}}(P, \omega_S, \omega_p, \tau_D, \tau_N, x) \tag{17}$$

$$\begin{aligned} R'_{\mathrm{Neel}}(P, \omega_S, \omega_I, \tau_D, \tau_N, x) = {} & \frac{L(x)}{x}(13PJ_F(\omega_S, \tau_D, \tau_N) \\ & + 7(1-P)J_F(\omega_I, \tau_D, \tau_N) + 6(1-P)J_F(0, \tau_D, \tau_N)) \\ & + \left(1 - 2\frac{L(x)}{x} - L^2(x)\right)(3J_F(\omega_I, \tau_D, \tau_N) + 4J_F(0, \tau_D, \tau_N)) \\ & + L^2(x)(3J_A(\omega_I, \tau_D) + 4J_A(0, \tau_D)). \end{aligned} \tag{18}$$

The corresponding curve is shown in Figure 5(a) and can be compared to the analogous longitudinal NMRD profile: the variation between the r_1 and r_2 curves are well correlated and, as expected, r_2 reaches a plateau at high magnetic fields.

The dominant Brownian rotation model can also be extended to transverse relaxation and is given by Ref 57

$$R_2^* = \frac{1}{T_2^*} = \frac{16\pi}{135}\left(\frac{\mu_0}{4\pi}\right)^2 \mu_{\mathrm{SPM}}^2 \gamma_p^2 \frac{C}{R_{\mathrm{NMR}} D}$$

$$R'_{\mathrm{Brown}}(\omega_p, \tau_D, \tau_\perp, \tau_\parallel, x) \tag{19}$$

FIGURE 3 | Nuclear magnetic relaxation dispersion (NMRD) profiles predicted by the low anisotropy model (dominant Néel relaxation). If not explicitly mentioned the used parameters are: R_{SPM} = 5 nm, $D = 3 \times 10^{-9}$ m^2 s^{-1}, $M_{\mathrm{sat}} = 2 \times 10^5$ A m^{-1}, C_{Fe} = 1 mM, $\tau_N = 10^{-9}$ s, and P = 0.8. (a) NMRD profiles for different radii. The circled last inflection point is shifted to a low magnetic field when the radius increases. (b) When the saturation magnetization increases, the maximum position is shifted to lower fields. (c) The region of influence of the different parameters on the curve.

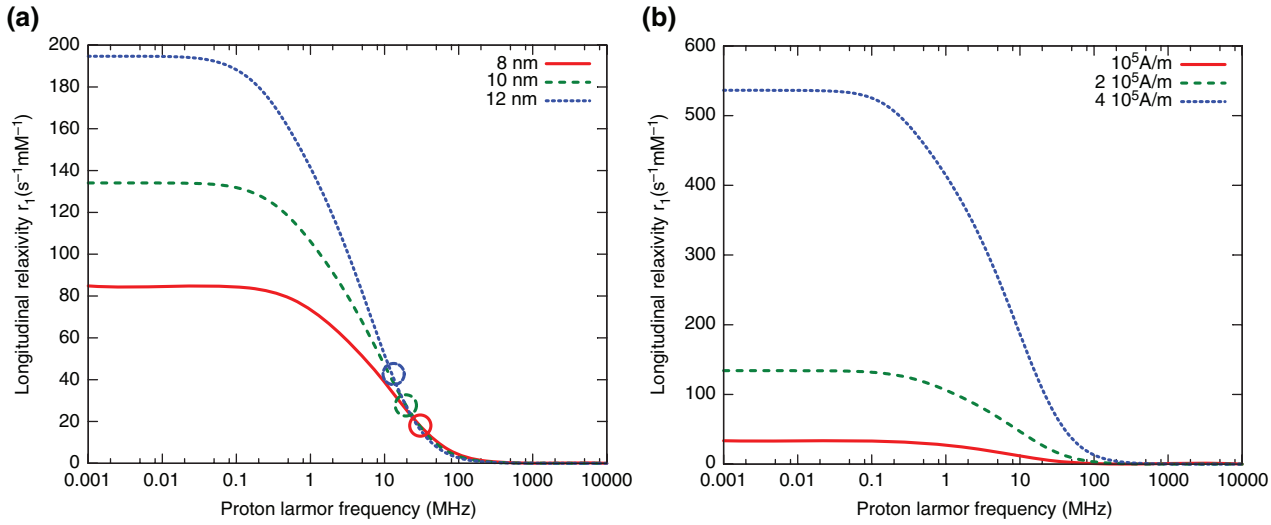

FIGURE 4 | Nuclear magnetic relaxation dispersion (NMRD) profiles of the Rigid Dipole relaxation model for (a) different radii R_{SPM} and (b) different magnetizations M_{sat} for magnetite. If not explicitly mentioned on the graph, the used parameters are: $R_{SPM} = 10$ nm, $D = 3 \times 10^{-9}$ m^2 s^{-1}, $M_{sat} = 2 \times 10^5$ A m^{-1}, $C_{Fe} = 1$ mM, $T = 310$ K, and $\eta = 0.6915$ Pa s. In (a), the last inflection point of each curve is also circled.

$$R'_{\text{Brown}}(\omega_p,\tau_D,\tau_\perp,\tau_\parallel,x) = L^2(x)\left(4J_A(0,\tau_D)+3J_A(\omega_p,\tau_D)\right)$$

$$+\left(1-\frac{2L(x)}{x}-L^2(x)\right)\left(4J_F(0,\tau_\parallel)+3J_F(\omega_I,\tau_\parallel)\right)$$

$$+\frac{L(x)}{x}\left(6J_F(0,\tau_\perp)+7J_F(\omega_p,\tau_\perp)\right). \qquad (20)$$

The corresponding curve is illustrated in Figure 5(b).

These equations are deduced from the Redfield formalism, so that they are—strictly speaking—only valid in the MAR (Eq. (7)) and for a free-induction decay (FID) sequence. Nevertheless, if the echo time τ_{echo} (defined as the time between the 90°-pulse and the first 180°-pulse) is longer than the correlation time—i.e., $\tau_{echo} > \tau_D$ which is usually the case in the MAR—the corresponding transverse relaxation rate will also be equal to Eq. (19) for a Carr-Purcell-Meiboom-Gill (CPMG) or a spin echo sequence, i.e., $R_2^* = R_2^{SE} = R_2^{CPMG}$.

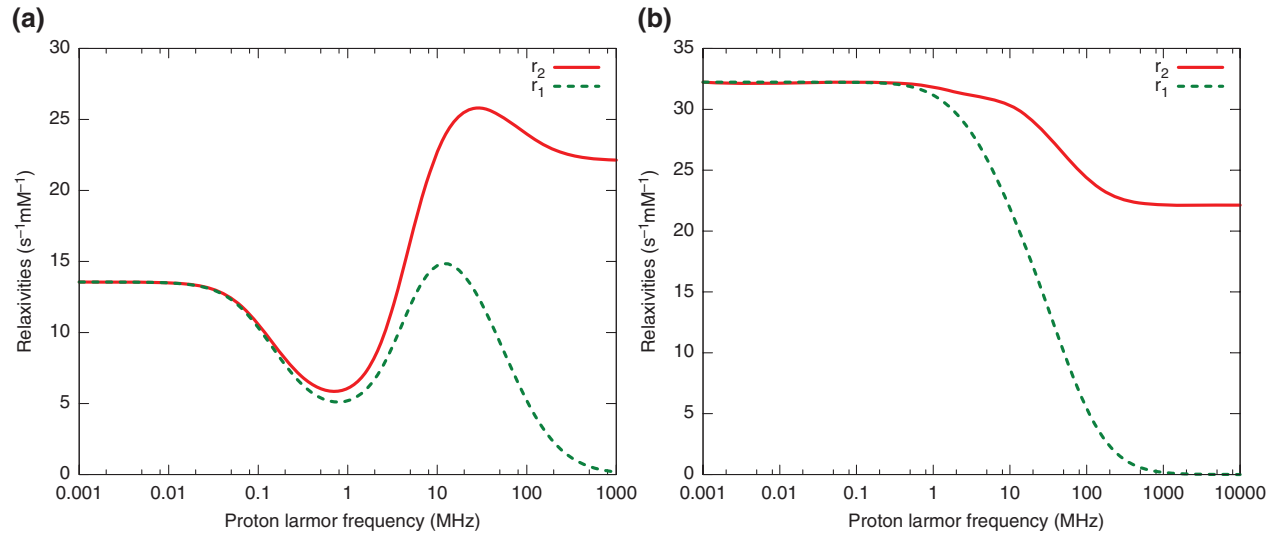

FIGURE 5 | Nuclear magnetic relaxation dispersion (NMRD) profiles for the transverse relaxation for (a) the low anisotropy model and (b) the Rigid Dipole model. Parameters used for the graphs: $R_{SPM} = 5$ nm, $D = 3 \times 10^{-9}$ m^2 s^{-1}, $M_{sat} = 2 \times 10^5$ A m^{-1}, $C_{Fe} = 1$ mM, $T = 310$ K, $\eta = 0.6915$ Pa s, $\tau_N = 10^{-9}$ s, and $P = 0.8$.

Unfortunately, those equations do not seem able to match the experimental results for transverse relaxation. Indeed, recent studies have shown that it was not possible to fit longitudinal *and* transverse NMRDs at the same time—indicating that a relaxation mechanism may miss in the models, at least for the transverse relaxation rate.[55,56,58] Moreover, most of the experimental R_2-NMRDs seem to exhibit a monotonously increase of R_2 with B_0 while the theoretical predictions predict a decrease of R_2 before it reaches a plateau.

The missing mechanism may be for example the one described by the 'three-phase iron model'[44,59]: this model is able to fit T_1 and T_2 NMRD profiles at the same time. In this model, relaxation is supposed to have three contributions (see Ref 44 for more details):

$$R_1 = F_S R_{1S} + F_P R_{1P} \tag{21}$$

$$R_2 = F_S R_{2S} + F_P R_{2P} + F_s R_{2s}. \tag{22}$$

Indeed, one SPM nanoparticle is supposed to be composed of three phases: one superparamagnetic core, antiferromagnetic inclusions in the core and a paramagnetic phase. Including an empirical expression for R_{2S}, the authors are able to fit all their T_1 and T_2 NMRDs. However, applying this model necessitates a significant additional number of parameters and a strong hypothesis on the NP structure which should ideally be asserted by other independent measurement methods such as magnetometry, TEM, or XRD for example.

Calculating Relaxivities

To ease the comparison between different types of sample, relaxation rates are often normalized by the magnetic compound concentration—this ratio is called 'relaxivity.' For example, in the case of iron oxide NPs, relaxation rates are divided by the iron concentration of the sample and are expressed in $(\text{mM[Fe]})^{-1}\ \text{s}^{-1}$. Relaxivity provides a quantitative information on the contrast efficiency of the NP: the larger its value is, the more efficient the CA. For the case of iron oxide Fe_yO_z, the SPM NP concentration C can be expressed as

$$C = \frac{N_{\text{SPM}}}{V_{\text{sample}}} = \frac{C_{\text{Fe}}}{1000} \frac{(56y + 16z)}{V_{\text{crystal}} \rho_{\text{Fe}_y\text{O}_z} y} \tag{23}$$

where V_{crystal} is the volume of the nanocrystal, $\rho_{\text{Fe}_y\text{O}_z}$ is its mass density, both expressed in MKS units. C_{Fe} is the iron concentration in the sample expressed in mM[Fe]. Relaxivities can then be obtained easily, replacing C by Eq. (23) in the expression of the relaxation rates and taking $C_{\text{Fe}} = 1$ mM[Fe]. The relaxivities of different samples of SPM NPs are provided in Table 2.

Transverse Relaxation at High Fields

At the high magnetic field B_0, the longitudinal relaxation rate always tends to zero while the transverse relaxation rate converges to a value called 'secular term.' This condition is reached when

TABLE 2 | Relaxivities of Different Samples of SPM NPs

		Name	r_1 (s^{-1} mM^{-1}[Fe])	r_2 (s^{-1} mM^{-1}[Fe])	r_2/r_1
Previous Commercial Contrast Agents	SPIO	SHU-555A (Resovist)[60]	25.4 (0.47 T, 37°C)	151	5.94
		AMI-25 (Endorem)[43]	9.95 (1.5 T, 37°C)	158	16
		AMI-25 (Endorem)[61]	25 (0.4 T, 37°C)	147	5.88
			23.7 (0.47 T, 39°C)	107	4.51
	USPIO	AMI-227 (Sinerem)[43]	19.5 (1.5 T, 37°C)	87.6	4.49
		AMI-227 (Sinerem)[61]	46.9 (0.4 T, 37°C)	88.2	1.88
			22.7 (0.47 T, 39°C)	53.1	2.34
		MION-46 L[62]	22.2 (0.47 T, 35°C)	43.7	1.97
		NC100150 (Clariscan)[63]	24.0 (0.47 T, 35°C)	36.4	1.64
Potential CAs Reported in Literature	Cluster c1c2c3c4paa5k[45]		25 (1 T, 37°C)	427	17
	Condense cluster[64]		/	512 (1.4 T, 37°C)	/
	Magneto-polymeric-nanohybrids using ($MnFe_2O_4$)[65]		/	567 (1.5 T, 25°C)	/

CA, contrast agents; SPIO, superparamagnetic particles of iron oxide; SPM NP, superparamagnetic nanoparticle; USPIO, ultrasmall particles of iron oxide.

$$\omega_p \tau_D = \gamma_p B_0 \frac{R_{NMR}^2}{D} > 1. \quad (24)$$

At such fields, the SPM magnetic moment is blocked along the applied magnetic field—the Brownian and Néel relaxation times are infinite—which leads to mathematical simplifications.

Scaling Law in the MAR

Both Eqs (17) and (19) tend to the same expression when B_0 tends to infinity, which yields

$$R_2^* = \frac{1}{T_2^*} = \frac{64\pi}{135}\left(\frac{\mu_0}{4\pi}\right)^2 \mu_{SPM}^2 \gamma_p^2 \frac{C}{R_{NMR} D}. \quad (25)$$

This expression is only valid in the MAR. For single SPM nanocrystals, Eq. (25) can be expressed as a scaling law of the minimal distance of approach and of the magnetization. In the case of iron oxide NPs, it can be written as

$$R_2^* = b C_{Fe} R_{NMR}^2 \left(M_{NMR}^{sat}\right)^2 \quad (26)$$

b is a constant which depends on the diffusion coefficient and the nature of the NPs. For magnetite at 37°C, it was experimentally determined that $b = 46.4\ 10^{-12}$ when d was expressed in nm and M_{NMR}^{sat} in A m^{-1}.[45] That value is double the theoretical prediction ($b_{theoretical} = 23.6\ 10^{-12}$)—the reasons for this are still unclear. This expression shows that, in the MAR, r_2 quadratically increases with increasing radius and magnetization.

FID in the SDR

When the size (or the magnetization) of the nanoparticle increases, if the condition

$$\frac{\gamma_p \mu_0 M_{NMR}^{sat} R_{SPM}^2}{3D} \gg 1 \quad (27)$$

is fulfilled, the nanoparticle properties are out of the MAR and the previous equations are not valid anymore. The system is in the 'static dephasing regime' (SDR). The more the size increases, the more the protons seem static during the relaxation compared to the NPs. In this case, the ergodic assumption is not valid anymore and the Redfield formalism cannot be used. This regime is called the 'static regime' and the corresponding transverse relaxation rate is given by Ref 39

$$\frac{1}{T_2^*} = \frac{2\pi\mu_0}{9\sqrt{3}} C \gamma_p \mu_{SPM}. \quad (28)$$

This expression is independent of the NP size and is only related to the NP concentration and its magnetic moment. It is also easy to show that the corresponding relaxivity only depends on the NP's effective magnetization M_{NMR}^{sat}.

Partial Refocusing Model (CPMG Sequence) in the SDR

For a CPMG sequence, when the system is in the SDR condition (Eq. (27)), the partial refocusing model must be used. The transverse relaxation in this case is given by

$$\frac{1}{T_2^{CPMG}} = 3\pi x^{1/3} C D R_{NMR} \left[1.34 + \frac{4\pi C R_{NMR}^3}{3} x\right]^{5/3};$$

$$x = \sqrt{\frac{1}{20}} \gamma_I \mu_0 \frac{\mu_{SPM}}{\pi R_{NMR}^3} \tau_{echo} \quad (29)$$

where τ_{echo} is the echo time—i.e., the time interval between the 90° and the first 180° pulses.

In this model, contrary to the MAR, r_2 decreases with increasing radius, while it increases when the echo time gets longer.

Spin Echo Model

A recent work by Kurz et al.[41] has led to the expression of a transverse relaxation equation obtained by a spin echo sequence in the static regime. They predicted that the maximum of the echo exponentially decays with an increasing echo time and is characterized by a relaxation rate given by

$$\frac{1}{T_2} = \frac{1}{\tau}\left[1 - \left[\mathrm{Re}\left(\frac{1-f}{G(f\tau\delta\omega) - fG(\tau\delta\omega)}\right)\right]^{-1}\right] \quad (30)$$

with

$$\tau = \frac{1}{\kappa}\frac{R_{SPM}^2}{D}\ ;\ \kappa \approx \frac{126 f^{2/3}\left[1 - f^{5/3}\right]}{18 - f^{2/3}\left[7 - 7f - 18 f^{5/3}\right]}\ ;$$

$$G(z) = \frac{1}{3} + \frac{2}{3}[1 - 2iz]\sqrt{\frac{1}{3}\left[1 - \frac{i}{z}\right]}\,\mathrm{arcoth}\left(\sqrt{\frac{1}{3}\left[1 - \frac{i}{z}\right]}\right);$$

$$f = C\frac{4}{3}\pi R_{NMR}^3;$$

$$\delta\omega = \frac{1}{3}\gamma_p \mu_0 M_{NMR}^{sat} \quad (31)$$

This equation should be valid in all usually considered regimes, i.e., motional averaging and static regimes. It is obtained supposing that the correlation time is short enough compared to the measurement time, i.e., $\tau \ll T_2$.[41,66] The expression given for κ is an approximation of the solution of a transcendental equation (see Ref 41 for more information). However, even with the exact value of κ, an agreement within the MAR range (Figure 6) was not achieved in this present study with the simulations. The very low value of f compared to the value used in Ref 41 may explain this discrepancy.

Simulations

As there is no simple analytical equation able to describe the relaxation in the whole radius or magnetization range, many studies use simulations to predict relaxation rates. Simulations can be used as accurate validation tools for the existing models and are able to consider more complex and realistic systems, such as clustered NPs, water diffusion constrained in geometrical tubes, SPM labeled cells, etc.

Nuclear Magnetic Relaxation Dispersion

To our knowledge, very few methods allow the simulation of a whole NMRD of a sample containing SPM NPs. In general, NMR simulations consist of numerically solving quantum equations which, in the case of relaxation, requires a lot of computer time. For relaxation, another method consists of simulating some correlation functions[67] but its validity is restricted by the Redfield condition (Eq. (7)).

We recently introduced a new method[19] allowing the simulation of relaxation in the case of SPM NPs, which is valid independently of the Redfield condition. This method is an extension of the T_2 simulations (see below) and is not too time consuming. It was shown that each regime (SDR or MAR) was characterized by its own scaling laws and that bigger particles (larger than 40 nm) could not be experimentally detected: the last NMRD inflection point is shifted to a proton Larmor frequency low enough to cancel the relaxation rate at usual imaging frequencies.

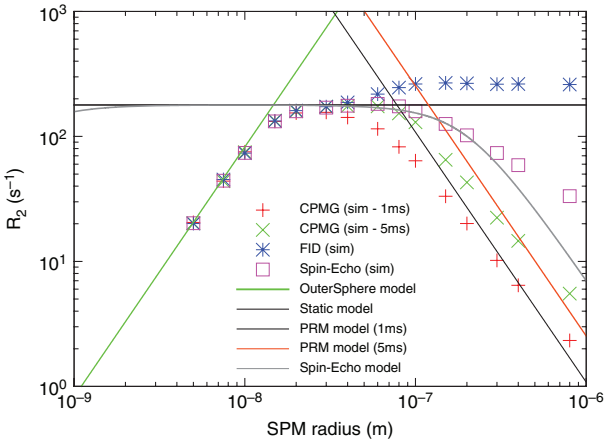

FIGURE 6 | Simulation results and theoretical prediction of the transverse relaxation rate at a high magnetic field. Each model fits well its region of validity except for the spin echo model which seems to fit only the static dephasing regime (SDR) regime (the value of $\kappa = 0.002395$ for f = 3.14 10^{-6} was obtained by numerically solving the transcendental equation in Ref 41).

T_2 at High Magnetic Field

Contrary to NMRD, many simulations have been carried out to predict the value of T_2 at high magnetic fields (secular term) for more than 25 years.[42,68] These types of simulations are less time consuming and are based on the classical idea that under a local magnetic field, the spin rotates around that field at the local Larmor frequency. Magnetic inhomogeneities in the sample lead to spin dephasing which results in the relaxation phenomenon.

In these simulations, in the case of SPM NPs, proton diffusion is modeled by a random walk and thousands of trajectories are simulated to obtain the average proton magnetization. CPMG, FID, or spin echo sequences can be easily implemented. This method was first applied to homogeneously distributed particles and shows the different behaviors of the MAR and the SDR.[36,37] Simulation results and model predictions are shown in Figure 6. The R_2 dependence on the radius follows a bell curve which describes a transition from the MAR to the SDR. In the MAR, R_2 increases with the particle size and then reaches a plateau predicted by the static model. For the CPMG and spin echo cases, the relaxation rates then decrease because of the 180° pulses which partially refocus the spins. This decrease depends on the inter-echo time in the CPMG case. In the case of the FID, the relaxation rate becomes independent of the radius in the SDR. This curve shows that there is an optimal size to gain a maximum (secular) relaxation rate (see Table 3). In the case of magnetite, the optimal radius is about 20 nm which, from the experimental point of view, is a challenge to synthesize without aggregation and precipitation.

TABLE 3 | Theoretical Prediction of the Maximum r_2 Achievable for Different Types of Superparamagnetic Particles[45]

	M_v (A m^{-1})	Optimal Radius (nm)	Predicted r_2 (s^{-1} mM^{-1})
Maghemite Particles	350,000	22	750
Clusters of Maghemite Particles (Volume Dilution of 5)	70,000	60	750
Iron–Iron Oxide Core Shell Particles	660,000	19	1200
Zn–Mn Ferrite Particles	875,000	17	1860

Clustering

In the last decade, more elaborate CAs have been developed to increase contrast efficiency, or to make them suitable for multimodal imaging.[69,70] These CAs are entities which can comprise several nanocrystals and can be coated by an impermeable layer (Figure 7). Clustering nanocrystals can occur both *in vitro* and *in vivo*, which could influence the relaxation rate, and finally, the efficiency, of the CAs.[71,72]

In such cases, the models must be modified to take NP aggregation into account. Several experimental and theoretical studies have been devoted to understanding and predicting these systems' behavior.[73–76] Depending on the nanocrystal or aggregation sizes, clustering can lead to an increase or decrease in the relaxation rate. For the secular term, this can be qualitatively understood through Figure 6. An initial clustering of nanocrystals in the MAR leads to a larger effective cluster radius and thus to an increase of the R_2. If the aggregation is too large, the effective cluster will be in the SDR and R_2 will then decrease.

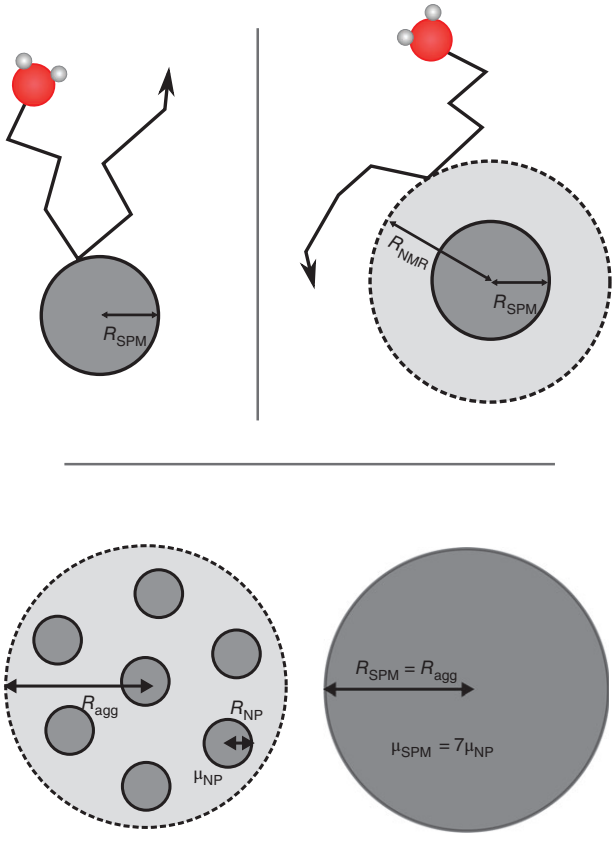

FIGURE 7 | Clustered and unclustered systems with their associated parameters.

More quantitatively, these kinds of systems can be treated as a single particle with an appropriate size and magnetic moment (Figure 7). If we consider an aggregate composed of N_{agg} nanocrystals of size R_{SPM} and magnetic moment μ_{NP}, and with an aggregate effective minimal distance of approach of R_{agg}, R_{NMR} must be replaced by R_{agg} and the magnetic moment μ_{SPM} must be taken as the sum of all the NP magnetic moments, i.e., $\mu_{SPM} = N_{agg}\mu_{NP}$. It is less clear what must be replaced in the Langevin function: if the NPs interact with each other in each entity, then $\mu_{SPM} = N_{agg}\mu_{NP}$ should be a good approximation, otherwise, it is $\mu_{SPM} = \mu_{NP}$ which should define x. The particle concentration C must also be replaced by an aggregate concentration: if a number of N_{agg}^{tot} clusters composes the sample,

$$C = \frac{N_{agg}^{tot}}{V_{sample}} = \frac{C_{NP}}{Nagg} \tag{32}$$

which can be related to the nanoparticle concentration in the sample C_{NP}.

COMPARISON WITH EXPERIMENTS

Nuclear Magnetic Relaxation Dispersion

NMRD is now used as a characterization method for samples containing SPM NPs. Equation (9) is often

used with four fitting parameters (SPM radius, magnetization, Néel time, and P) to extract the sample properties.[50,77,78] The obtained experimental minimal distance of approach is often in the range between the TEM and the hydrodynamic sizes (obtained by dynamic light scattering for example).[21–23] The extracted Néel time seems to be qualitatively correlated to the Néel time obtained by AC-susceptibility but can be several orders of magnitude different.[47] The model was also successfully tested in different solvents, at different temperatures or with different viscosities.[53,55,79] Recently, transverse NMRDs have also been obtained.[54,55] If the experimental shapes of the curves were qualitatively similar to the theoretical predictions, it was not possible to fit longitudinal and transverse NMRDs with the low anisotropy model at once.

R_2

The models predicting the transverse secular term have also been largely tested. The scaling law (Eq. (26)) predicted in the MAR was checked in our previous work, which compiles a lot of data from the literature.[45] A square dependence on the radius was observed but the coefficient was larger than expected. In the static regime, the partial refocusing model was also successfully qualitatively tested.[80] The trends predicted by the simulations for aggregation or for different particle shapes have also been well reproduced.[73,81–84]

Experimental Discrepancies

While the experimental results are qualitatively well described by theory, some discrepancies remain when a more precise quantitative study is made. As the relaxation rates are highly dependent on the NP size (or magnetization), a small difference in size (or magnetization) can lead to a non-negligible variation of the relaxation rates. As a consequence, size polydispersity[85] is often mentioned to justify the disagreement between experimental and theoretical values. Partial aggregation in a sample can also lead to a modification of the relaxation times. This often appears as an evolution of T_2 with time, during the measurement.[73,86] The nature of the coating is also known to influence the proton minimal distance of approach and thus the relaxation rates.[22,23] Some authors also claim that there could be an exchange between the surface and the bulk water and introduce additional fitting parameters in the models.[23] However, it has not yet been established that such an exchange exists.

When cells are labeled by SPM NPs, the experimental relaxation rates greatly decrease compared to the relaxation rates that the particles induce when they are homogeneously distributed in water.[71,87–89] This is of importance for *in vivo* applications as the particles can be efficient in water alone, but can drastically lose this efficiency *in vivo*. This decrease of R_2 can be understood by a large aggregation of the NPs and by the water compartmentalization due to the cells—but no accurate model describes this case yet.

BIOMEDICAL APPLICATIONS OF SUPERPARAMAGNETIC NANOPARTICLES

Superparamagnetic magnetite/maghemite particles, used as MRI contrast enhancers, are classified into two main categories whose applications are different:

1. Superparamagnetic particles of iron oxide (SPIO) containing several magnetite crystals within the same (permeable or impermeable) coating. Their hydrodynamic size is larger than 40 nm. Standard SPIOs are injected intravenously. However, some of them, intended for gastrointestinal imaging and coated within an insoluble and non-biodegradable matrix, are administered orally.
2. Ultrasmall particles of iron oxide (USPIO): particles containing a single magnetite crystal and whose hydrodynamic size is smaller than 40 nm. This type of agent is always injected intravenously.

Maghemite/magnetite CAs (principally SPIOs) were first used 30 years ago for liver imaging. Thanks to the capture of the nanoparticles by Kupffer cells, a major shortening of the transverse relaxation time is observed in liver tissue[90–92] causing negative contrast because of the large r_2/r_1 ratio of SPIOs. Moreover, the signal loss due to this relaxation enhancement is selective, since the particles are not internalized in lesions (void of Kupffer cells), which facilitates the early detection of tumors. Such particles are also captured by the spleen[93] and lymph nodes.[94]

For applications necessitating a longer blood half-life (MR angiography, tissue perfusion imaging,

molecular imaging, etc.), SPIOs are not efficient due to their fast capture by the liver which is related to their rather large hydrodynamic size. USPIOs are better candidates since they stay in the blood longer. Moreover, because of their relaxation properties and especially because of their smaller r_2/r_1 ratio, they can be used as positive CAs for T_1-weighted imaging.[95–99]

However, the use of magnetic particles in routine clinical MRI has drastically decreased in recent years. Most of the SPM CAs have been withdrawn from the market, except those intended for imaging the gastrointestinal track.[100]

Current applications of maghemite particles in MRI are more related to research in cellular and molecular MR imaging.[101–104] Bulte et al.[6] defined molecular imaging as 'the non-invasive and repetitive imaging of targeted macromolecules and biological processes' and cellular imaging as 'the non-invasive and repetitive imaging of targeted cells and cellular processes.' After grafting a suited vector onto a usual CA, this new type of imaging makes it possible to target specific processes, such as atherosclerosis,[105] apoptosis,[104] amyloid deposition in Alzheimer's disease,[103] etc. The main problem is getting a large quantity of a CA directly to the targeted zone of the body, in order to obtain a sufficient contrast during the imaging experiment. Magnetite nanoparticles are excellent candidates as base elements for designing molecular or cellular imaging CAs. Their transverse relaxivity is far larger than that of gadolinium chelates and each targeted particle contains many thousands of iron atoms. The MR effect is thus optimum. However, for a good sensitivity they must be used as a negative CA, which induces some specificity problems because of the occurrence of artifacts in T_2 and T_2* weighted images.

SPM NPs are also naturally present in the human body and are stored in ferritin, which can naturally influence the MRI contrast (see Box 2).

BOX 2

FERRITIN: THE MAGNETIC PROTEIN

Ferritin is the iron storing protein of mammals. It is constituted of 24 protein subunits forming a 13 nm spherical shell. Inside ferritin, iron is stored as a ferrihydrite ($5Fe_2O_3$-$9H_2O$) nano crystal.[106] Ferrihydrite is antiferromagnetic: it contains two sublattices of Fe^{3+} ions whose resultant magnetic moments are in opposite directions and cancel each other out.[107] However, for nanoparticles of ferrihydrite—such as that present inside ferritin—the compensation is not perfect and a small magnetic moment remains for each particle. Because of the nanometric size of the crystal, this magnetic moment has a superparamagnetic behavior.[108] At a magnetic field of 1 T, the magnetisation of ferritin is almost two orders of magnitude smaller than that of magnetite particles. Therefore, the presence of ferritin can only be detected by MRI in regions where the protein significantly accumulates, like the liver, spleen, and even some nuclei of the brain.[109] Indeed ferritin causes a shortening of T_2 which results in hypointensities on T_2 and T_2* weighted images.[110,111] Many groups have tried to use this property to quantify ferritin *in vivo* by MRI with mitigated results.[112–115] The effect on T_1 is almost negligible. It has been shown that the transverse relaxation of water protons in the presence of ferritin is due to an exchange of protons between the surface of the ferrihydrite crystal and bulk water,[116] which is clearly different from the relaxation induced by magnetite particles. Moreover, the transverse relaxivity of ferritin is very small compared to that of magnetite nanoparticles, but it increases with the field.[117] This increase is linear in aqueous solutions while it can be either linear or quadratic in iron containing tissues, possibly because of protein clustering or degradation into hemosiderin.[118]

CONCLUSION

Since SPM particles are extensively used as MRI CAs for molecular and cellular imaging, a good understanding of the proton relaxation they induce is needed. Different theoretical models have been developed in order to describe the relaxation mechanism in different situations corresponding to different particle sizes, magnetizations, or different solvent diffusion properties. All these models are conditioned by hypotheses and assumptions that must be carefully taken into account. These theories have been validated thanks to the comparison of their predictions with experimental and computer simulation results. However, the understanding of the relaxation induced by SPM particles *in vivo* is still hazy since their distribution in cells and tissues is not homogeneous because of clustering. This point merits further study.

REFERENCES

1. Pankhurst QA, Connolly J, Jones SK, Dobson J. Applications of magnetic nanoparticles in biomedicine. *J Phys Appl Phys* 2003, 36:R167–R181. doi:10.1088/0022-3727/36/13/201.
2. Sensenig R, Sapir Y, MacDonald C, Cohen S, Polyak B. Magnetic nanoparticle-based approaches to locally target therapy and enhance tissue regeneration *in vivo*. *Nanomed* 2012, 7:1425–1442. doi:10.2217/nnm.12.109.
3. Tran N, Webster TJ. Magnetic nanoparticles: biomedical applications and challenges. *J Mater Chem* 2010, 20:8760. doi:10.1039/c0jm00994f.
4. Jordan A, Scholz R, Wust P, Fähling H, Felix R. Magnetic fluid hyperthermia (MFH): cancer treatment with AC magnetic field induced excitation of biocompatible superparamagnetic nanoparticles. *J Magn Magn Mater* 1999, 201:413–419. doi:10.1016/S0304-8853(99)00088-8.
5. Knopp T, Buzug TM. *Magnetic Particle Imaging: An Introduction to Imaging Principles and Scanner Instrumentation*. Berlin-Heidelberg, Germany: Springer; 2012.
6. Bulte JWM, Kraitchman DL. Iron oxide MR contrast agents for molecular and cellular imaging. *NMR Biomed* 2004, 17:484–499. doi:10.1002/nbm.924.
7. Gossuin Y, Gillis P, Hocq A, Vuong QL, Roch A. Magnetic resonance relaxation properties of superparamagnetic particles. *WIREs Nanomed Nanobiotechnol* 2009, 1:299–310. Available at: http://onlinelibrary.wiley.com/doi/10.1002/wnan.36/full (Accessed May 22, 2014).
8. Delangre S, Vuong QL, Po C, Gallez B, Gossuin Y. Theoretical and experimental study of ON-resonance saturation, an MRI sequence for positive contrast with superparamagnetic nanoparticles. *J Magn Reson* 2015, 252:151–162. doi:10.1016/j.jmr.2015.01.007.
9. Cunningham CH, Arai T, Yang PC, McConnell MV, Pauly JM, Conolly SM. Positive contrast magnetic resonance imaging of cells labeled with magnetic nanoparticles. *Magn Reson Med* 2005, 53:999–1005. doi:10.1002/mrm.20477.
10. Stuber M, Gilson WD, Schär M, Kedziorek DA, Hofmann LV, Shah S, Vonken EJ, Bulte JW, Kraitchman DL. Positive contrast visualization of iron oxide-labeled stem cells using inversion-recovery with ON-resonant water suppression (IRON). *Magn Reson Med* 2007, 58:1072–1077. doi:10.1002/mrm.21399.
11. Zurkiya O, Hu X. Off-resonance saturation as a means of generating contrast with superparamagnetic nanoparticles. *Magn Reson Med* 2006, 56:726–732. doi:10.1002/mrm.21024.
12. du Trémolet de Lacheisserie E, Gignoux D, Schlenker M. *Magnetism*. New York: Springer Science & Business Media; 2005.
13. Dormann JL. Le phénomène de superparamagnétisme. *Rev Phys Appliquée* 1981, 16:275–301. doi:10.1051/rphysap:01981001606027500.
14. Bean CP, Livingston JD. Superparamagnetism. *J Appl Phys* 1959, 30:S120. doi:10.1063/1.2185850.
15. Néel L. Theory of the magnetic after-effect in ferromagnetics in the form of small particles with applications to baked clays. *Ann Geophys (CNRS)* 1949, 5:99–136.
16. Kötitz R, Fannin PC, Trahms L. Time domain study of Brownian and Néel relaxation in ferrofluids. *J Magn Magn Mater* 1995, 149:42–46. doi:10.1016/0304-8853(95)00333-9.
17. Respaud M. Magnetization process of noninteracting ferromagnetic cobalt nanoparticles in the superparamagnetic regime: deviation from Langevin law. *J Appl Phys* 1999, 86:556. doi:10.1063/1.370765.
18. Hanson M, Johansson C, Morup S. The influence of magnetic anisotropy on the magnetization of small ferromagnetic particles. *J Phys Condens Matter* 1993, 5:725–732. doi:10.1088/0953-8984/5/6/009.
19. Vuong QL, Gossuin Y, Gillis P, Delangre S. New simulation approach using classical formalism to water nuclear magnetic relaxation dispersions in presence of superparamagnetic particles used as MRI contrast agents. *J Chem Phys* 2012, 137:114505. doi:10.1063/1.4751442.
20. Rorschach HE. A classical theory of NMR relaxation processes. *J Magn Reson* 1986, 1969:519–530. Available at: http://www.sciencedirect.com/science/article/pii/0022236486903884 (Accessed August 7, 2014).
21. Di Marco M, Sadun C, Port M, Guilbert I, Couvreur P, Dubernet C. Physicochemical characterization of ultrasmall superparamagnetic iron oxide particles (USPIO) for biomedical application as MRI contrast agents. *Int J Nanomedicine* 2007, 2:609. Available at: http://www.ncbi.nlm.nih.gov/pmc/articles/pmc2676801/ (Accessed June 12, 2014).
22. Carroll MRJ, Huffstetler PP, Miles WC, Goff JD, Davis RM, Riffle JS, House MJ, Woodward RC, St Pierre TG. The effect of polymer coatings on proton transverse relaxivities of aqueous suspensions of magnetic nanoparticles. *Nanotechnology* 2011, 22:325702. doi:10.1088/0957-4484/22/32/325702.

23. LaConte LE, Nitin N, Zurkiya O, Caruntu D, O'Connor CJ, Hu X, Bao G. Coating thickness of magnetic iron oxide nanoparticles affects R2 relaxivity. *J Magn Reson Imaging* 2007, 26:1634–1641. doi:10.1002/jmri.21194.
24. Renshaw PF, Owen CS, McLaughlin AC, Frey TG, Leigh JS. Ferromagnetic contrast agents: a new approach. *Magn Reson Med* 1986, 3:217–225. Available at: http://onlinelibrary.wiley.com/doi/10.1002/mrm.1910030205/abstract (Accessed July 31, 2014).
25. Solomon I, Bloembergen N. Nuclear magnetic interactions in the HF molecule. *J Chem Phys* 1956, 25:261. doi:10.1063/1.1742867.
26. Bloembergen N, Purcell E, Pound R. Relaxation effects in nuclear magnetic resonance absorption. *Phys Rev* 1948, 73:679–712. doi:10.1103/PhysRev.73.679.
27. Lauffer RB. Paramagnetic metal complexes as water proton relaxation agents for NMR imaging: theory and design. *Chem Rev* 1987, 87:901–927. Available at: http://pubs.acs.org/doi/abs/10.1021/cr00081a003 (Accessed August 4, 2014).
28. Kowalewski J, Kruk D, Parigi G. NMR relaxation in solution of paramagnetic complexes: recent theoretical progress for $S \geq 1$. *Adv Inorg Chem* 2005, 57:41–104.
29. Gillis P, Koenig SH. Transverse relaxation of solvent protons induced by magnetized spheres: application to ferritin, erythrocytes, and magnetite. *Magn Reson Med* 1987, 5:323–345. doi:10.1002/mrm.1910050404.
30. Koenig SH, Brown RD. Field-cycling relaxometry of protein solutions and tissue: implications for MRI. *Prog Nucl Magn Reson Spectrosc* 1990, 22:487–567. doi:10.1016/0079-6565(90)80008-6.
31. Roch A, Muller RN. Longitudinal relaxation of water protons in colloidal suspensions of superparamagnetic crystal. In: *Proceedings of the 11th Annual Meeting of the Society of Magnetic Resonance in Medicine, Works in Progress* 1447, 1992.
32. Koenig SH, Kellar KE. Theory of 1/T1 and 1/T2 NMRD profiles of solutions of magnetic nanoparticles. *Magn Reson Med* 1995, 34:227–233. Available at: http://onlinelibrary.wiley.com/doi/10.1002/mrm.1910340214/full (Accessed August 5, 2014).
33. Roch A, Muller RN, Gillis P. Water relaxation by SPM particles: neglecting the magnetic anisotropy? A caveat. *J Magn Reson Imaging* 2001, 14:94–96. Available at: http://onlinelibrary.wiley.com/doi/10.1002/jmri.1157/full (Accessed May 5, 2014).
34. Roch A, Muller RN, Gillis P. Theory of proton relaxation induced by superparamagnetic particles. *J Chem Phys* 1999, 110:5403–5411. Available at: http://scitation.aip.org/content/aip/journal/jcp/110/11/10.1063/1.478435 (Accessed August 5, 2014).
35. Lévy M, Gazeau F, Wilhelm C, Neveu S, Devaud M, Levitz P. Revisiting MRI contrast properties of nanoparticles: beyond the superparamagnetic regime. *J Phys Chem C* 2013, 117:15369–15374. doi:10.1021/jp404199f.
36. Brooks RA, Moiny F, Gillis P. OnT2-shortening by weakly magnetized particles: the chemical exchange model. *Magn Reson Med* 2001, 45:1014–1020. doi:10.1002/mrm.1135.
37. Gillis P, Moiny F, Brooks RA. OnT2-shortening by strongly magnetized spheres: a partial refocusing model. *Magn Reson Med* 2002, 47:257–263. doi:10.1002/mrm.10059.
38. Yung K-T. Empirical models of transverse relaxation for spherical magnetic perturbers. *Magn Reson Imaging* 2003, 21:451–463. Available at: http://www.sciencedirect.com/science/article/pii/S0730725X02006409 (Accessed August 6, 2014).
39. Brown RJ. Distribution of fields from randomly placed dipoles: free-precession signal decay as result of magnetic grains. *Phys Rev* 1961, 121:1379. Available at: http://journals.aps.org/pr/abstract/10.1103/PhysRev.121.1379 (Accessed August 5, 2014).
40. Yablonskiy DA, Haacke EM. Theory of NMR signal behavior in magnetically inhomogeneous tissues: the static dephasing regime. *Magn Reson Med* 1994, 32:749–763. Available at: http://onlinelibrary.wiley.com/doi/10.1002/mrm.1910320610/full (Accessed August 6, 2014).
41. Kurz FT, Kampf T, Heiland S, Bendszus M, Schlemmer H-P, Ziener CH. Theoretical model of the single spin-echo relaxation time for spherical magnetic perturbers: spin-echo relaxation time for spherical magnetic perturbers. *Magn Reson Med* 2014, 71:1888–1895. doi:10.1002/mrm.25196.
42. Hardy PA, Henkelman RM. Transverse relaxation rate enhancement caused by magnetic particulates. *Magn Reson Imaging* 1989, 7:265–275. Available at: http://www.sciencedirect.com/science/article/pii/0730725X89905493 (Accessed June 16, 2014).
43. Bulte JW, Vymazal J, Brooks RA, Pierpaoli C, Frank JA. Frequency dependence of MR relaxation times II. Iron oxides. *J Magn Reson Imaging* 1993, 3:641–648. doi:10.1002/jmri.1880030414.
44. Bulte JWM, Brooks RA, Moskowitz BM, Bryant LH, Frank JA. Relaxometry, magnetometry, and EPR evidence for three magnetic phases in the MR contrast agent MION-46L. *J Magn Magn Mater* 1999, 194:217–223. doi:10.1016/S0304-8853(98)00555-1.
45. Vuong QL, Berret J-F, Fresnais J, Gossuin Y, Sandre O. A universal scaling law to predict the efficiency of magnetic nanoparticles as MRI T2-contrast agents. *Adv Healthc Mater* 2012, 1:502–512. doi:10.1002/adhm.201200078.
46. Abragam A. *The Principles of Nuclear Magnetism*. London, UK: Oxford University Press; 2006.

47. Bordonali L, Kalaivani T, Sabareesh KP, Innocenti C, Fantechi E, Sangregorio C, Casula MF, Lartigue L, Larionova J, Guari Y. NMR-D study of the local spin dynamics and magnetic anisotropy in different nearly monodispersed ferrite nanoparticles. *J Phys Condens Matter* 2013, 25:66008. doi:10.1088/0953-8984/25/6/066008.

48. Freed JH. Dynamic effects of pair correlation functions on spin relaxation by translational diffusion in liquids. II. Finite jumps and independent T1 processes. *J Chem Phys* 1978, 68:4034. doi:10.1063/1.436302.

49. Ayant Y, Belorizky E, Aluzon J, Gallice J. Calcul des densités spectrales résultant d'un mouvement aléatoire de translation en relaxation par interaction dipolaire magnétique dans les liquides. *J Phys* 1975, 36:991–1004. doi:10.1051/jphys:01975003601009910O.

50. Laurent S, Forge D, Port M, Roch A, Robic C, Vander Elst L, Muller RN. Magnetic iron oxide nanoparticles: synthesis, stabilization, vectorization, physicochemical characterizations, and biological applications. *Chem Rev* 2008, 108:2064–2110. doi:10.1021/cr068445e.

51. Batlle X, Labarta A. Finite-size effects in fine particles: magnetic and transport properties. *J Phys Appl Phys* 2002, 35:R15–R42. doi:10.1088/0022-3727/35/6/201.

52. CRC handbook of chemistry and physics: a ready-reference book of chemical and physical data. Cleveland, Ohio: CRC Press; 1976.

53. Bulte JWM, Brooks RA, Moskowitz BM, Bryant LH Jr, Frank JA. T1 and T2 relaxometry of monocrystalline iron oxide nanoparticles (MION-46L): theory and experiment. *Acad Radiol* 1998, 5 (suppl 1): S137–S140. doi:10.1016/S1076-6332(98)80084-6.

54. Arosio P, Thévenot J, Orlando T, Orsini F, Corti M, Mariani M, Bordonali L, Innocenti C, Sangregorio C, Oliveira H, et al. Hybrid iron oxide-copolymer micelles and vesicles as contrast agents for MRI: impact of the nanostructure on the relaxometric properties. *J Mater Chem B* 2013, 1:5317. doi:10.1039/c3tb00429e.

55. Gossuin Y, Orlando T, Basini M, Henrard D, Lascialfari A, Mattea C, Stapf S, Vuong QL. NMR relaxation induced by iron oxide particles: testing theoretical models. *Nanotechnology* 2016, 27:155706. doi:10.1088/0957-4484/27/15/155706.

56. Basini M, Orlando T, Arosio P, Casula MF3, Espa D, Murgia S, Sangregorio C, Innocenti C, Lascialfari A. Local spin dynamics of iron oxide magnetic nanoparticles dispersed in different solvents with variable size and shape: a ^{1}H NMR study. *J Chem Phys* 2017, 146:34703. doi:10.1063/1.4973979.

57. Rollet AL, Neveu S, Porion P, Dupuis V, Cherrak N, Levitz P. New approach for understanding experimental NMR relaxivity properties of magnetic nanoparticles: focus on cobalt ferrite. *Phys Chem Chem Phys* 2016, 18:32981–32991. doi:10.1039/C6CP06012A.

58. Orlando T, Albino M, Orsini F, Innocenti C, Basini M, Arosio P, Sangregorio C, Corti M, Lascialfari A. On the magnetic anisotropy and nuclear relaxivity effects of Co and Ni doping in iron oxide nanoparticles. *J Appl Phys* 2016, 119:134301. doi:10.1063/1.4945026.

59. Bulte JW, Brooks RA, Moskowitz BM, Bryant LH, Frank JA. Relaxometry and magnetometry of the MR contrast agent MION-46L. *Magn Reson Med* 1999, 42:379–384.

60. Wang Y-XJ, Hussain SM, Krestin GP. Superparamagnetic iron oxide contrast agents: physicochemical characteristics and applications in MR imaging. *Eur Radiol* 2001, 11:2319–2331. doi:10.1007/s003300100908.

61. Jung CW, Jacobs P. Physical and chemical properties of superparamagnetic iron oxide MR contrast agents: ferumoxides, ferumoxtran, ferumoxsil. *Magn Reson Imaging* 1995, 13:661–674. doi:10.1016/0730-725X(95)00024-B.

62. Koenig SH, Kellar KE, Fujii DK, Gunther WH, Briley-Saebø K, Spiller M. Three types of physical measurements needed to characterize iron oxide nanoparticles for MRI and MRA. *Acad Radiol* 2002, 9:S5–S10. doi:10.1016/S1076-6332(03)80386-0.

63. Kellar KE, Fujii DK, Gunther WH, Briley-Saebø K, Bjørnerud A, Spiller M, Koenig SH. NC100150 injection, a preparation of optimized iron oxide nanoparticles for positive-contrast MR angiography. *J Magn Reson Imaging* 2000, 11:488–494. doi:10.1002/(SICI)1522-2586(200005)11:5<488::AID-JMRI4>3.0.CO;2-V.

64. Xie X, Zhang C. Controllable assembly of hydrophobic superparamagnetic iron oxide nanoparticle with mPEG-PLA copolymer and its effect on MR transverse relaxation rate. *J Nanomater* 2011, 2011:1–7. doi:10.1155/2011/152524.

65. Yang J, Lee CH, Ko HJ, Suh JS, Yoon HG, Lee K, Huh YM, Haam S. Multifunctional magneto-polymeric nanohybrids for targeted detection and synergistic therapeutic effects on breast cancer. *Angew Chem Int Ed* 2007, 46:8836–8839. doi:10.1002/anie.200703554.

66. Bauer WR, Nadler W, Bock M, Schad LR, Wacker C, Hartlep A, Ertl G. Theory of the BOLD effect in the capillary region: an analytical approach for the determination of T2 in the capillary network of myocardium. *Magn Reson Med* 1999, 41:51–62. Available at: http://bio.physik.uni-wuerzburg.de/people/kh/Bauer%20et%20al.%20MRM%201999(2).pdf (Accessed October 20, 2014).

67. Grivet J-P. NMR relaxation parameters of a Lennard-Jones fluid from molecular-dynamics simulations.

J Chem Phys 2005, 123:34503. doi:10.1063/1.1955447.

68. Majumdar S, Gore J. Studies of diffusion in random fields produced by variations in susceptibility. *J Magn Reson* 1988, 1969:41–55. doi:10.1016/0022-2364(88)90155-2.
69. Bao N, Gupta A. Self-assembly of superparamagnetic nanoparticles. *J Mater Res* 2011, 26:111–121. doi:10.1557/jmr.2010.25.
70. Douziech-Eyrolles L, Marchais H, Hervé K, Munnier E, Soucé M, Linassier C, Dubois P, Chourpa I. Nanovectors for anticancer agents based on superparamagnetic iron oxide nanoparticles. *Int J Nanomedicine* 2007, 2:541. Available at: http://www.ncbi.nlm.nih.gov/pmc/articles/pmc2676819/ (Accessed June 16, 2014).
71. Lévy M, Wilhelm C, Devaud M, Levitz P, Gazeau F. How cellular processing of superparamagnetic nanoparticles affects their magnetic behavior and NMR relaxivity: magnetic and NMR behaviors of cell-processed USPIO. *Contrast Media Mol Imaging* 2012, 7:373–383. doi:10.1002/cmmi.504.
72. Kostopoulou A, Velu SK, Thangavel K, Orsini F, Brintakis K, Psycharakis S, Ranella A, Bordonali L, Lappas A, Lascialfari A. Colloidal assemblies of oriented maghemite nanocrystals and their NMR relaxometric properties. *Dalton Trans* 2014, 43:8395. doi:10.1039/c4dt00024b.
73. Roch A, Gossuin Y, Muller RN, Gillis P. Superparamagnetic colloid suspensions: water magnetic relaxation and clustering. *J Magn Magn Mater* 2005, 293:532–539. doi:10.1016/j.jmmm.2005.01.070.
74. Vuong QL, Gillis P, Gossuin Y. Monte Carlo simulation and theory of proton NMR transverse relaxation induced by aggregation of magnetic particles used as MRI contrast agents. *J Magn Reson* 2011, 212:139–148. doi:10.1016/j.jmr.2011.06.024.
75. Matsumoto Y, Jasanoff A. T2 relaxation induced by clusters of superparamagnetic nanoparticles: Monte Carlo simulations. *Magn Reson Imaging* 2008, 26:994–998. doi:10.1016/j.mri.2008.01.039.
76. Brown KA, Vassiliou CC, Issadore D, Berezovsky J, Cima MJ, Westervelt RM. Scaling of transverse nuclear magnetic relaxation due to magnetic nanoparticle aggregation. *J Magn Magn Mater* 2010, 322:3122–3126. doi:10.1016/j.jmmm.2010.05.044.
77. Forge D, Gossuin Y, Roch A, Laurent S, Elst LV, Muller RN. Development of magnetic chromatography to sort polydisperse nanoparticles in ferrofluids. *Contrast Media Mol Imaging* 2010, 5:126–132. doi:10.1002/cmmi.374.
78. Félix-González N, Urbano-Bojorge AL, Mina-Rosales A, del Pozo-Guerrero F, Serrano-Olmedo JJ. Assessment of a heuristic model for characterization of magnetic nanoparticles as contrast agent in MRI. *Concepts Magn Reson Part A* 2015, 44A:279–286. doi:10.1002/cmr.a.21361.
79. Kruk D, Korpała A, Taheri SM, Kozłowski A, Förster S, Rössler EA. 1H relaxation enhancement induced by nanoparticles in solutions: influence of magnetic properties and diffusion. *J Chem Phys* 2014, 140:174504. doi:10.1063/1.4871461.
80. Chen D-X, Taboada E, Roig A. Experimental study on T2 relaxation time of protons in water suspensions of iron-oxide nanoparticles: cases of composite nanospheres. *J Magn Magn Mater* 2011, 323:2487–2492. doi:10.1016/j.jmmm.2011.05.022.
81. Balasubramaniam S, Kayandan S, Lin YN, Kelly DF, House MJ, Woodward RC, St Pierre TG, Riffle JS, Davis RM. Toward design of magnetic nanoparticle clusters stabilized by biocompatible diblock copolymers for T_2-weighted MRI contrast. *Langmuir* 2014, 30:1580–1587. doi:10.1021/la403591z.
82. Hak S, Goa PE, Stenmark S, Bjerkholt FF, Haraldseth O. Transverse relaxivity of iron oxide nanocrystals clustered in nanoemulsions: experiment and theory: T2 relaxivity of iron oxide clusters. *Magn Reson Med* 2015, 74:858–867. doi:10.1002/mrm.25465.
83. Van Roosbroeck R, Van Roy W, Stakenborg T, Trekker J, D'Hollander A, Dresselaers T, Himmelreich U, Lammertyn J, Lagae L. Synthetic antiferromagnetic nanoparticles as potential contrast agents in MRI. *ACS Nano* 2014, 8:2269–2278. doi:10.1021/nn406158h.
84. Pöselt E, Kloust H, Tromsdorf U, Janschel M, Hahn C, Maßlo C, Weller H. Relaxivity optimization of a PEGylated iron-oxide-based negative magnetic resonance contrast agent for T_2-weighted spin–echo imaging. *ACS Nano* 2012, 6:1619–1624. doi:10.1021/nn204591r.
85. Carroll MRJ, Woodward RC, House MJ, Teoh WY, Amal R, Hanley TL, St Pierre TG. Experimental validation of proton transverse relaxivity models for superparamagnetic nanoparticle MRI contrast agents. *Nanotechnology* 2010, 21:35103. doi:10.1088/0957-4484/21/3/035103.
86. Sun N, Chen D-X, Gu H-C, Wang X-L. Experimental study on relaxation time of protons in water suspensions of iron-oxide nanoparticles: waiting time dependence. *J Magn Magn Mater* 2009, 321:2971–2975. doi:10.1016/j.jmmm.2009.04.073.
87. Billotey C, Wilhelm C, Devaud M, Bacri JC, Bittoun J, Gazeau F. Cell internalization of anionic maghemite nanoparticles: quantitative effect on magnetic resonance imaging. *Magn Reson Med* 2003, 49:646–654. doi:10.1002/mrm.10418.
88. Simon GH, Bauer J, Saborovski O, Fu Y, Corot C, Wendland MF, Daldrup-Link HE. T1 and T2 relaxivity of intracellular and extracellular USPIO at 1.5T and 3T clinical MR scanning. *Eur Radiol* 2006, 16:738–745. doi:10.1007/s00330-005-0031-2.

89. Bowen CV, Zhang X, Saab G, Gareau PJ, Rutt BK. Application of the static dephasing regime theory to superparamagnetic iron-oxide loaded cells. *Magn Reson Med* 2002, 48:52–61. doi:10.1002/mrm.10192.

90. Ros PR, Freeny PC, Harms SE, Seltzer SE, Davis PL, Chan TW, Stillman AE, Muroff LR, Runge VM, Nissenbaum MA, et al. Hepatic MR imaging with ferumoxides: a multicenter clinical trial of the safety and efficacy in the detection of focal hepatic lesions. *Radiology* 1995, 196:481–488. doi:10.1148/radiology.196.2.7617864.

91. Arnold P, Ward J, Wilson D, Ashley Guthrie J, Robinson PJ. Superparamagnetic iron oxide (SPIO) enhancement in the cirrhotic liver: a comparison of two doses of ferumoxides in patients with advanced disease. *Magn Reson Imaging* 2003, 21:695–700. doi:10.1016/S0730-725X(03)00101-2.

92. Kehagias DT, Gouliamos AD, Smyrniotis V, Vlahos LJ. Diagnostic efficacy and safety of MRI of the liver with superparamagnetic iron oxide particles (SH U 555 A). *J Magn Reson Imaging* 2001, 14:595–601. doi:10.1002/jmri.1224.

93. Kreft BP, Tanimoto A, Leffler S, Finn JP, Oksendal AN, Stark DD. Contrast-enhanced MR imaging of diffuse and focal splenic disease with use of magnetic starch microspheres. *J Magn Reson Imaging* 1994, 4:373–379. doi:10.1002/jmri.1880040324.

94. Anzai Y, Blackwell KE, Hirschowitz SL, Rogers JW, Sato Y, Yuh WT, Runge VM, Morris MR, McLachlan SJ, Lufkin RB. Initial clinical experience with dextran-coated superparamagnetic iron oxide for detection of lymph node metastases in patients with head and neck cancer. *Radiology* 1994, 192:709–715. doi:10.1148/radiology.192.3.7520182.

95. Bjørnerud A, Johansson L. The utility of superparamagnetic contrast agents in MRI: theoretical consideration and applications in the cardiovascular system: superparamagnetic contrast agents. *NMR Biomed* 2004, 17:465–477. doi:10.1002/nbm.904.

96. Bjerner T, Johansson L, Wikström G, Ericsson A, Briley-Soebo K, Bjørnerud A, Ahlström H. In and ex vivo MR evaluation of acute myocardial ischemia in pigs by determining R1 in steady state after the administration of the intravascular contrast agent NC100150 injection. *Invest Radiol* 2004, 39:479–486. doi:10.1097/01.rli.0000128658.63611.b3.

97. Sandiford L, Phinikaridou A, Protti A, Meszaros LK, Cui X, Yan Y, Frodsham G, Williamson PA, Gaddum N, Botnar RM, et al. Bisphosphonate-anchored PEGylation and radiolabeling of superparamagnetic iron oxide: long-circulating nanoparticles for *in vivo* multimodal (T1 MRI-SPECT) imaging. *ACS Nano* 2013, 7:500–512. doi:10.1021/nn3046055.

98. Chambon C, Clement O, Le Blanche A, Schouman-Claeys E, Frija G. Superparamagnetic iron oxides as positive MR contrast agents: in vitro and in vivo evidence. *Magn Reson Imaging* 1993, 11:509–519. doi:10.1016/0730-725X(93)90470-X.

99. Kellar KE, Fujii DK, Gunther WH, Briley-Saebø K, Bjornerod A, Spiller M, Koenig SH. Important considerations in the design of iron oxide nanoparticles as contrast agents for Tl-weighted MRI and MRA. *Acad Radiol* 2002, 9:S34–S37. doi:10.1016/S1076-6332(03)80391-4.

100. Ittrich H, Peldschus K, Raabe N, Kaul M, Adam G. Superparamagnetic iron oxide nanoparticles in biomedicine: applications and developments in diagnostics and therapy. *RöFo Fortschritte Auf Dem Geb Röntgenstrahlen Bildgeb Verfahr* 2013, 185:1149–1166. doi:10.1055/s-0033-1335438.

101. Sharifi S, Seyednejad H, Laurent S, Atyabi F, Saei AA, Mahmoudi M. Superparamagnetic iron oxide nanoparticles for *in vivo* molecular and cellular imaging: SPIONs for molecular and cellular imaging. *Contrast Media Mol Imaging* 2015, 10:329–355. doi:10.1002/cmmi.1638.

102. Bulte JW, Douglas T, Witwer B, Zhang SC, Strable E, Lewis BK, Zywicke H, Miller B, van Gelderen P, Moskowitz BM. Magnetodendrimers allow endosomal magnetic labeling and in vivo tracking of stem cells. *Nat Biotechnol* 2001, 19:1141–1147. doi:10.1038/nbt1201-1141.

103. Wadghiri YZ, Sigurdsson EM, Sadowski M, Elliott JI, Li Y, Scholtzova H, Tang CY, Aguinaldo G, Pappolla M, Duff K, Wisniewski T, et al. Detection of Alzheimer's amyloid in transgenic mice using magnetic resonance microimaging. *Magn Reson Med* 2003, 50:293–302. doi:10.1002/mrm.10529.

104. Zhao M, Beauregard DA, Loizou L, Davletov B, Brindle KM. Non-invasive detection of apoptosis using magnetic resonance imaging and a targeted contrast agent. *Nat Med* 2001, 7:1241–1244. doi:10.1038/nm1101-1241.

105. Jaffer FA, Nahrendorf M, Sosnovik D, Kelly KA, Aikawa E, Weissleder R. Cellular imaging of inflammation in atherosclerosis using magnetofluorescent nanomaterials. *Mol Imaging* 2006, 5:85–92.

106. Harrison PM, Arosio P. The ferritins: molecular properties, iron storage function and cellular regulation. *Biochim Biophys Acta BBA Bioenerg* 1996, 1275:161–203. doi:10.1016/0005-2728(96)00022-9.

107. Néel L. Superparamagnétisme des grains très fins antiferromagnétiques. *C R Acad Sci* 1961, 252:4075–4080.

108. Kilcoyne SH, Cywinski R. Ferritin: a model superparamagnet. *J Magn Magn Mater* 1995, 140–144:1466–1467. doi:10.1016/0304-8853(94)00626-1.

109. Gossuin Y, Muller RN, Gillis P. Relaxation induced by ferritin: a better understanding for an improved

MRI iron quantification. *NMR Biomed* 2004, 17:427–432. doi:10.1002/nbm.903.

110. Doyle FH, Pennock JM, Banks LM, McDonnell MJ, Bydder GM, Steiner RE, Young IR, Clarke GJ, Pasmore T, Gilderdale DJ. Nuclear magnetic resonance imaging of the liver: initial experience. *Am J Roentgenol* 1982, 138:193–200. doi:10.2214/ajr.138.2.193.
111. Drayer B, Burger P, Darwin R, Riederer S, Herfkens R, Johnson GA. MRI of brain iron. *Am J Roentgenol* 1986, 147:103–110. doi:10.2214/ajr.147.1.103.
112. Brittenham GM, Badman DG, National Institute of Diabetes and Digestive and Kidney Diseases (NIDDK) Workshop. Noninvasive measurement of iron: report of an NIDDK workshop. *Blood* 2003, 101:15–19. doi:10.1182/blood-2002-06-1723.
113. Chen JC, Hardy PA, Clauberg M, Joshi JG, Parravano J, Deck JH, Henkelman RM, Becker LE, Kucharczyk W. T2 values in the human brain: comparison with quantitative assays of iron and ferritin. *Radiology* 1989, 173:521–526. doi:10.1148/radiology.173.2.2798884.
114. Bulte JWM, Miller GF, Vymazal J, Brooks RA, Frank JA. Hepatic hemosiderosis in non-human primates: quantification of liver iron using different field strengths. *Magn Reson Med* 1997, 37:530–536. doi:10.1002/mrm.1910370409.
115. Vymazal J, Brooks RA, Baumgarner C, Tran V, Katz D, Bulte JW, Bauminger R, Di Chiro G. The relation between brain iron and NMR relaxation times: an in vitro study. *Magn Reson Med* 1996, 35:56–61. doi:10.1002/mrm.1910350108.
116. Gossuin Y, Roch A, Muller RN, Gillis P, Lo Bue F. Anomalous nuclear magnetic relaxation of aqueous solutions of ferritin: an unprecedented first-order mechanism. *Magn Reson Med* 2002, 48:959–964. doi:10.1002/mrm.10316.
117. Vymazal J, Brooks RA, Zak O, McRill C, Shen C, Di Chiro G. T1 and T2 of ferritin at different field strengths: effect on MRI. *Magn Reson Med* 1992, 27:368–374. doi:10.1002/mrm.1910270218.
118. Hocq A, Luhmer M, Saussez S, Louryan S, Gillis P, Gossuin Y. Effect of magnetic field and iron content on NMR proton relaxation of liver, spleen and brain tissues: relaxation rates of liver, spleen and brain tissues. *Contrast Media Mol Imaging* 2015, 10:144–152. doi:10.1002/cmmi.1610.
119. Gleich B, Weizenecker J. Tomographic imaging using the nonlinear response of magnetic particles. *Nature* 2005, 435:1214–1217. doi:10.1038/nature03808.
120. Weizenecker J, Gleich B, Rahmer J, Dahnke H, Borgert J. Three-dimensional real-time *in vivo* magnetic particle imaging. *Phys Med Biol* 2009, 54:L1–L10. doi:10.1088/0031-9155/54/5/L01.
121. Markov DE, Boeve H, Gleich B, Borgert J, Antonelli A, Sfara C, Magnani M. Human erythrocytes as nanoparticle carriers for magnetic particle imaging. *Phys Med Biol* 2010, 55:6461–6473. doi:10.1088/0031-9155/55/21/008.
122. Bulte JWM, Gleich B, Weizenecker J, Bernard S, Walczak P, Borgert J, Aerts H, Boeve H. Developing cellular MPI: initial experience. In: *Proceedings of the ISMRM 16th Annual Meeting* 1675, 2008.
123. Bulte JWM, Walczak P, Janowski M, Krishnan KM, Arami H, Halkola A, Gleich B, Rahmer J. Quantitative 'hot-spot' imaging of transplanted stem cells using superparamagnetic tracers and magnetic particle imaging. *Tomography* 2015, 1:91–97. doi:10.18383/j.tom.2015.00172.